JGR Atmospheres

RESEARCH ARTICLE
10.1029/2021JD036035

This article is a companion to Fritts et al. (2022), https://doi.org/10.1002/2021JD035990.

Key Points:

- High spatial resolution of gravity wave dynamics at lower altitudes is critical in achieving realistic responses in the thermosphere
- Failure to describe gravity wave breaking dynamics significantly decreases secondary wave generation at smaller spatial scales
- Thermospheric secondary gravity waves excited by mountain waves in the winter hemisphere have dominant horizontal scales of ∼100–200 km

Supporting Information:

Supporting Information may be found in the online version of this article.

Correspondence to:

D. C. Fritts,
dave@gats-inc.com

Citation:

Fritts, D. C., Lund, A. C., Lund, T. S., & Yudin, V. (2022). Impacts of limited model resolution on the representation of mountain wave and secondary wave dynamics in local and global models: 2. Mountain wave and secondary wave evolutions in the thermosphere. *Journal of Geophysical Research: Atmospheres*, *127*, e2021JD036035. https://doi.org/10.1029/2021JD036035

Received 12 OCT 2021
Accepted 9 MAR 2022

Author Contributions:

Conceptualization: David C. Fritts
Data curation: Adam C. Lund, Thomas S. Lund
Formal analysis: Thomas S. Lund
Funding acquisition: David C. Fritts

Impacts of Limited Model Resolution on the Representation of Mountain Wave and Secondary Wave Dynamics in Local and Global Models: 2. Mountain Wave and Secondary Wave Evolutions in the Thermosphere

David C. Fritts[1,2], Adam C. Lund[2], Thomas S. Lund[1,3], and Valery Yudin[4]

[1]GATS, Boulder, CO, USA, [2]Embry-Riddle Aeronautical University, Daytona Beach, FL, USA, [3]University of Colorado, Boulder, CO, USA, [4]Catholic University of America, Washington, DC, USA

Abstract A companion paper by Fritts et al. (2022), https://doi.org/10.1002/2021JD035990 describes the consequences of decreasing horizontal resolution in the description of mountain wave (MW) propagation, breaking, and large-scale responses over the Southern Andes reaching into the mesosphere. This paper extends that analysis into the thermosphere, where MWs are confined below a critical level, but secondary gravity waves and acoustic waves become prominent and dominate the wave fields at higher altitudes. Like MWs at lower altitudes, the character and responses of secondary waves are strongly dependent on model resolution. MWs readily penetrate above a zonal wind minimum in the upper mesosphere and exhibit responses for varying resolution similar to those at lower altitudes. Both the MW and local mean responses weaken somewhat for resolution varying from 0.5 to 2 km, weaken more significantly for 4-km resolution, and fail to approximate the high-resolution results for 8-km resolution. MW momentum fluxes and induced local mean responses are very different than those in the mesosphere, but exhibit similar variability with coarsening resolution. Secondary gravity waves at larger scales arise due to MW-induced mean wind decelerations, hence are not highly sensitive to model resolutions of ∼0.5–2 km approximating MW breaking. However, acoustic waves are forced primarily by MW breaking, thus are poorly described at 2-km resolution and absent at 4-km resolution. These results reveal the dynamics that can and cannot be explicitly modeled as resolution is coarsened, and may aid in assessing, parameterizing, and/or compensating for the unresolved dynamics and their consequences.

Plain Language Summary This paper addresses the influences of decreasing resolution on the dynamics of secondary gravity waves (SGWs) arising in the thermosphere due to generation accompanying mountain wave (MW) breaking dynamics in the upper stratosphere and lower mesosphere. For high spatial resolution of 0.5 km able to describe the instability dynamics that account for MW breaking, SGW generation is strong and is driven by both (a) MW self-acceleration dynamics at larger spatial scales and (b) MW breaking dynamics at smaller spatial scales. Reductions in model resolution degrade the SGW responses in two ways: (a) decreasing resolution to 2 km removes the ability to describe MW breaking dynamics and weakens the smaller-scale SGW responses; and (b) decreasing resolution to 4 and 8 km significantly weakens or eliminates the larger-scale SGW responses in the thermosphere due to inadequate spatial resolution and/or numerical impacts on their phase and vertical group velocities.

1. Introduction

Gravity waves (GWs) arising from diverse sources at lower altitudes were recognized to penetrate into the mesosphere and lower thermosphere (MLT) over 60 years ago (Hines, 1960; Witt, 1962). Their ability to reach the thermosphere depends on the source character and altitudes, and the intervening winds that modulate their intrinsic phases speeds, $c_i = (c - U)$, for horizontal wind U and phase speed c along U. They are ubiquitous in the thermosphere (Djuth et al., 2004; Negrea & Zabotin, 2016; Oliver et al., 1997) and their major direct sources include deep convection (Azeem et al., 2015; Heale et al., 2020; Walterscheid et al., 2001), mountain waves (MWs) due to airflow over orography (Fritts et al., 2021; Lund et al., 2020; Smith et al., 2009, 2013), and inertia-GWs (IGWs) arising from jet stream and frontal imbalance and transience (Luo & Fritts, 1993; Plougonven & Snyder, 2007; Plougonven & Zhang, 2014; Sutherland et al., 2019; Vadas & Fritts, 2001; Yiğit et al., 2008).

Methodology: Adam C. Lund, Thomas S. Lund
Software: Adam C. Lund
Validation: Adam C. Lund
Visualization: Adam C. Lund
Writing – review & editing: David C. Fritts, Adam C. Lund, Valery Yudin

Another atmospheric source that becomes important as primary GWs from other lower atmosphere sources achieve large amplitudes is secondary GW (SGW) generation arising from local body forcing accompanying nonlinear "self-acceleration" (SA) dynamics of localized GW packets. These SA dynamics are especially important for GWs having small horizontal wavelengths, λ_h, large c_i, and large vertical group velocities, c_{gz}, because these exhibit the fastest and strongest evolutions. There is also now significant direct and indirect observational evidence for SGWs in the MLT that emphasizes their increasing importance at higher altitudes (Becker & Vadas, 2018, 2020; de Wit et al., 2017; Dong et al., 2021; Smith et al., 2013).

SA dynamics cause GW phase accelerations that steepen the GW phase at its leading edge (in altitude) because the GW resides in the region undergoing induced accelerations. This most often results in c_{gz} decreasing to zero, stalling of vertical propagation, and strong, transient forcing of a local three-dimensional (3-D) ΔU that projects onto larger-scale SGWs that rapidly propagate to higher and lower altitudes (Dong et al., 2020; Fritts et al., 2015, 2020). Additional SGWs and acoustic waves (AWs) are generated at smaller spatial scales due to GW breaking driven by large GW amplitudes accompanying SA dynamics. Specific evidence of 3-D responses to such SA dynamics in the PMC layer at ∼82 km, including larger- and smaller-scale SGWs, is provided by Dong et al. (2021). Importantly, the initial excitation of SGWs at larger scales precedes instabilities and breaking. Hence the smaller-scale dynamics are not fundamental to large-scale SGW generation, neither the larger- nor smaller-scale responses can be described quantitatively by linear GW theory, and the nonlinear SA generation mechanism represents a nonlinear revision of the initial linear theory by Luo and Fritts (1993) and Vadas and Fritts (2001, 2002).

Other thermospheric GWs arise from an initially surprising source. Long ocean surface infra-GWs also excite high-frequency acoustic GWs (AGWs) seen in the thermosphere and ionosphere at periods as short as ∼5 min, and as long as ∼3 hr (Djuth et al., 2004; Godin et al., 2015; Livneh et al., 2007). Tsunamis account for spectacular examples of these (Artru et al., 2005; Galvan et al., 2012; Komjathy et al., 2012; Laughman et al., 2017; Makela et al., 2011; Occhipinti et al., 2013). Thus, the mix of GWs from lower altitudes impacting thermosphere and ionosphere (TI) dynamics is certain to be highly geophysically, spatially, and temporally variable.

Our purposes here are to identify and quantify the implications of varying model resolution for thermospheric responses to MWs, SGWs, and AWs that arise from strong, nonlinear MW dynamics at lower altitudes as revealed in their amplitudes, scales, momentum fluxes, induced local-mean motions, and spectra from 80 to 180 km. This represents an extension of the analysis in the companion paper by Fritts et al. (2022; hereafter F22) addressing responses in the mesosphere. All these studies employed the Complex Geometry Compressible Atmosphere Model (CGCAM). The CGCAM simulation set-up and a brief review of the MW and secondary wave evolution obtained with 0.5-km resolution are provided in Sections 2 and 3. Section 4 describes the MW, SGW, and AW responses in the thermosphere extending those described by F22 at lower altitudes for model resolutions varying from 0.5 to 8 km. Horizontal cross sections of the vertical fluxes of horizontal momentum, $<u'w'>$, and the induced large-scale, zonal flow responses, $<\Delta U>$, for the varying resolutions are presented in Section 5. Section 6 examines the influences of decreasing resolution on the MW and SGW spectra averaged over earlier and later times. A discussion of these results with respect to previous studies, implications for global modeling of GW influences, and our conclusions are presented in Sections 7 and 8.

2. CGCAM Description

CGCAM results discussed here are the thermospheric responses derived from a suite of CGCAM simulations at progressively coarser resolutions. These are extensions of the initial high-resolution ($\Delta x = \Delta y = 0.5$ km) simulation examining the wave and mean-flow responses described by Lund et al. (2020, L20 hereafter) and Fritts et al. (2021, F21 hereafter). Those described by F22 and here were designed to explore the impacts of decreasing resolution on the fidelity of the MW, SGW, and AW responses in the thermosphere. The simulations employed initial conditions from a free-running WACCM simulation under winter conditions over the Southern Andes in a domain extending 2500 km in longitude and 2000 km in latitude. The model domain is shown at top in Figure 1 of F22. CGCAM employed variable resolution in x and y, with the highest resolution in each case extending 250 km in x and 750 km in y in a central domain over and in the lee of the major Southern Andes terrain. Terrain cross sections and spectra over the major terrain are shown as insets at top in Figure 1 of F22. Profiles of T_0, stability (N_0^2, for mean buoyancy frequency, N_0), and U_0 and V_0 are shown for reference in Figure 1. Altitudes

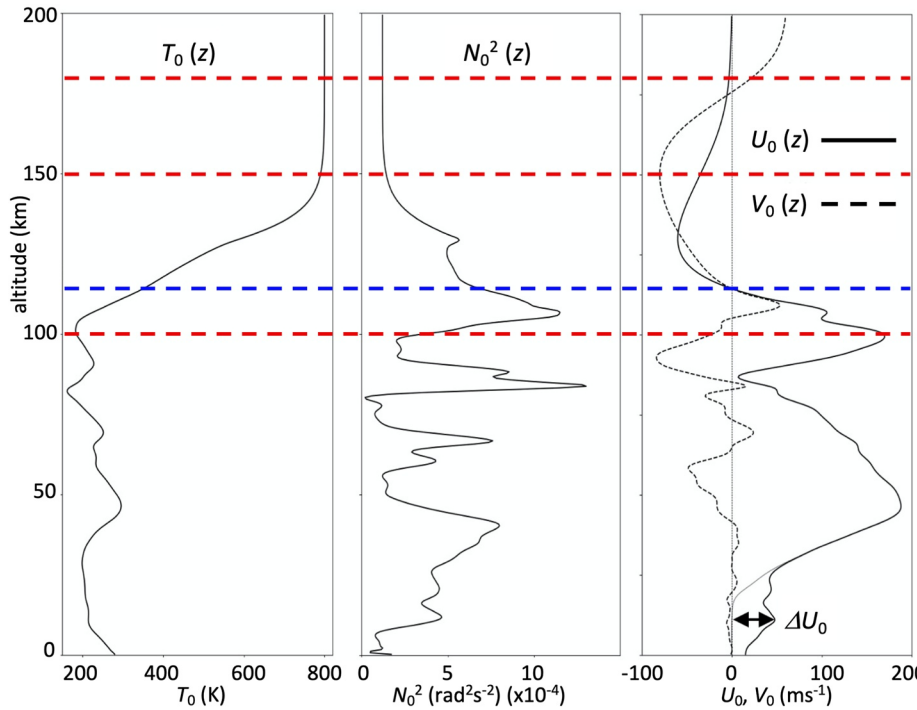

Figure 1. Initial profiles of T_0, N_0^2, U_0, and V_0. U_0 with ΔU_0 increasing to half its peak over 6 hr is indicated at bottom right (see Figure 2 in L20). Red dashed lines show the altitudes discussed below; the blue line shows the MW critical level at $z = 115$ km.

of horizontal cross sections discussed here, and the MW critical level, are shown in Figure 1 with red and blue dashed lines, respectively.

3. Overview of MW, SGW, and AW Dynamics and Evolutions at High Resolution

Results for isotropic $\Delta x = \Delta y = \Delta z = 0.5$ km resolution were described in detail by L20 and F21 and are illustrated for convenience with $u(x,z)$ and $u'(y,z)$ cross sections at 9 and 10 hr in Figure 2. For reference below, North Peak (NP) and South Peak (SP) are assumed to be 120 km north and south of the domain center. These fields exhibit the following responses relevant to our discussion of the implications of coarsening resolution below:

1. MW breaking over SP extends from $z \sim 40$ km to near the MW critical level at 115 km from ~9 to 10 hr,
2. MW breaking over NP occurs only above ~50 km and induces weaker responses than over SP,
3. Higher minimum breaking altitudes occur in the lee of lower terrain at other latitudes,
4. MW breaking begins at $x \sim 50$–100 km in the lee of SP and NP, and extends to larger x and upstream at higher altitudes at later times,
5. SGW and AW responses are strong at earlier times over SP and NP, but only achieve large amplitudes above the MW critical level ~2–3 scale heights, H, above the MW breaking altitudes,
6. Strong AWs are limited to regions within ~300 km of their sources, and
7. SGWs at higher altitudes have horizontal and vertical wavelengths, $\lambda_h \sim 70$–200 km and $\lambda_z \sim 50$ km or larger, at high altitudes, implying high intrinsic frequencies and rapid propagation.

Due to the MW critical level at 115 km, there are no steady-state primary MW responses at higher altitudes. Thus all the dynamics above 115 km are the result of (a) SGW and AW generation accompanying MW SA dynamics and breaking at lower altitudes and (b) induced larger-scale motions due to spatially-localized pseudo-momentum deposition that imposes 3-D responses extending into the thermosphere. Of these, AWs having roughly spherical phase fronts attain very high altitudes quickly due to their ~500 m s^{-1} phase speeds at higher altitudes. SGWs have large phase speeds, c, vertical wavelengths, λ_z, and c_{gz}, thus also quickly attain high altitudes.

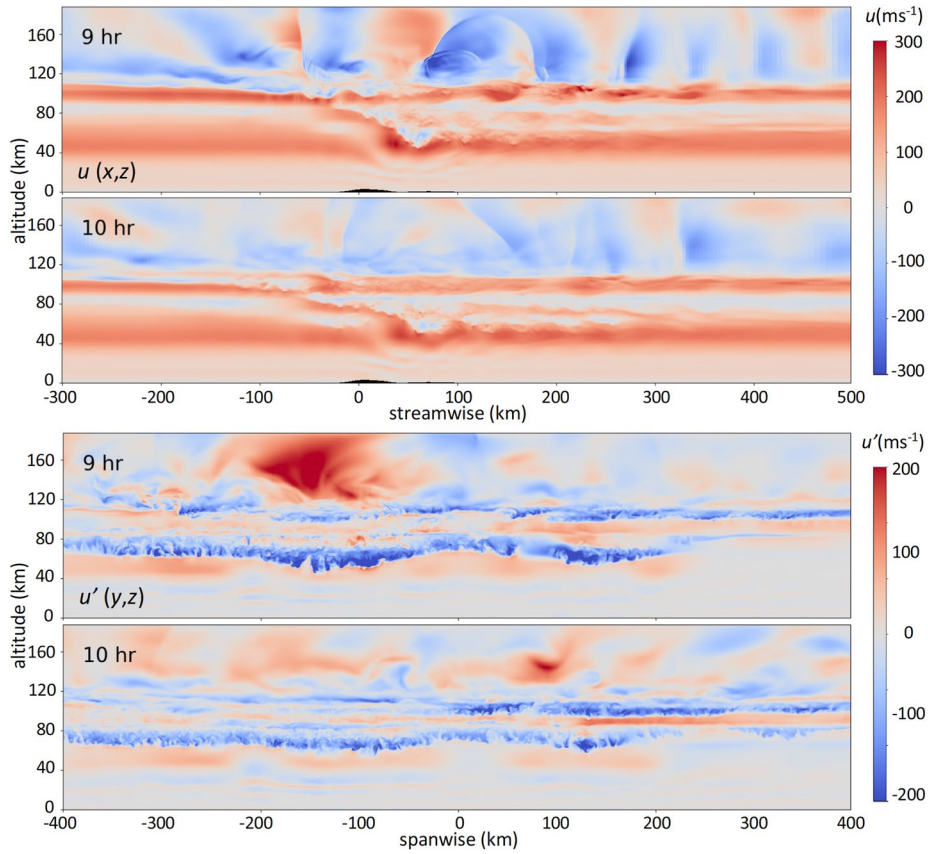

Figure 2. Responses of $u(x,z)$ across SP and $u'(y,z)$ at $x = 50$ km at 9 and 10 hr (top and bottom image sets). Note the large MW amplitudes in the mesosphere and very large SGW and AW amplitudes in the thermosphere.

Of particular relevance to our discussion below are the small primary MW $\lambda_x \sim 30$–60 km and their instability scales of ~3–5 km (see L20 and F21) that account for MW breaking, pseudo-momentum deposition, local 3-D body forcing, and SGW and AW generation arising from these dynamics. The major roles of small-scale dynamics accounting for the responses penetrating to higher altitudes will be seen below to account for strong sensitivity of the various thermospheric responses to decreasing model resolution.

4. Impacts of Decreasing Resolution on SGW and AW Responses in the Thermosphere

F22 described significant impacts of decreasing resolution on direct MW responses in the mesosphere, and attributed these to the decreasing ability of coarsening resolution to describe MW breaking dynamics sufficiently accurately. Results included reduced MW amplitudes, $<u'w'>$, and induced $<\Delta U>$, but those reduced responses nevertheless maintained roughly the same MW phases and regions of MW breaking. Here we examine the related responses in the thermosphere.

4.1. $u(x,z)$ and $u'(y,z)$

Thermospheric responses to reduced resolution are shown over SP in Figures 3 and 4 at 8, 9, 10, and 12 hr at altitudes from 80 to 180 km including the upper mesosphere having a MW critical level at $z = 115$ km. The impacts of decreasing resolution at these altitudes are similar in some respects to those for MW dynamics in the mesosphere described by F22. However, they also exhibit major differences because of the very different character of the SGW and AW sources compared to the MWs at lower altitudes.

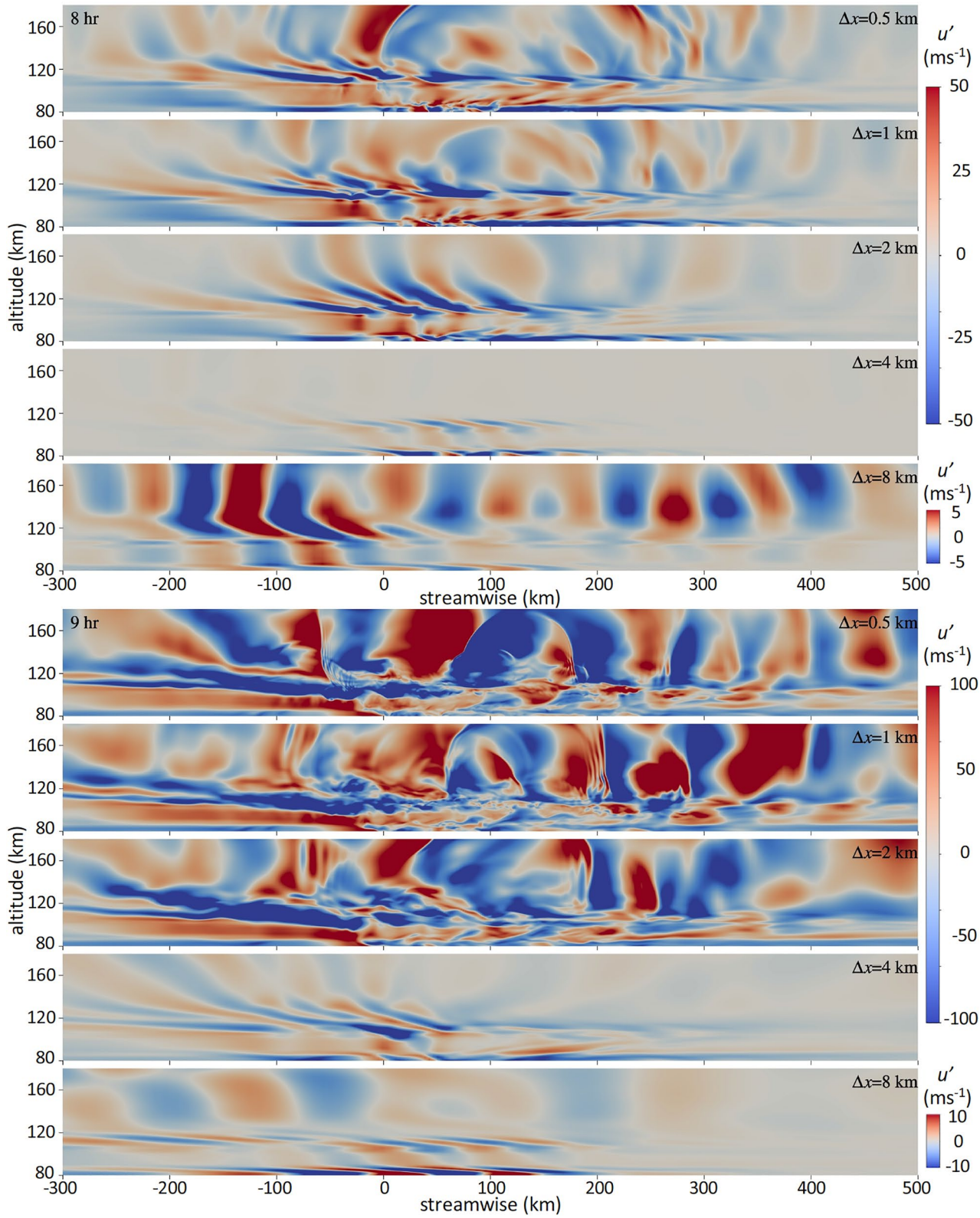

Figure 3. Streamwise-vertical cross sections of $u'(x,z)$ over SP at 8 and 9 hr (top and bottom image sets) showing comparisons of varying central resolutions of $\Delta x = \Delta y = 0.5$, 1, 2, 4, and 8 km (top to bottom) and $\Delta z = 0.5$ km in all cases. Note the large reductions of SGW and AW amplitudes as resolution coarsens to 2 km, the dramatic failure to even approximate the high-resolution thermospheric responses at $\Delta x = 4$ and 8 km, and the much smaller color scales for $\Delta x = 8$ km.

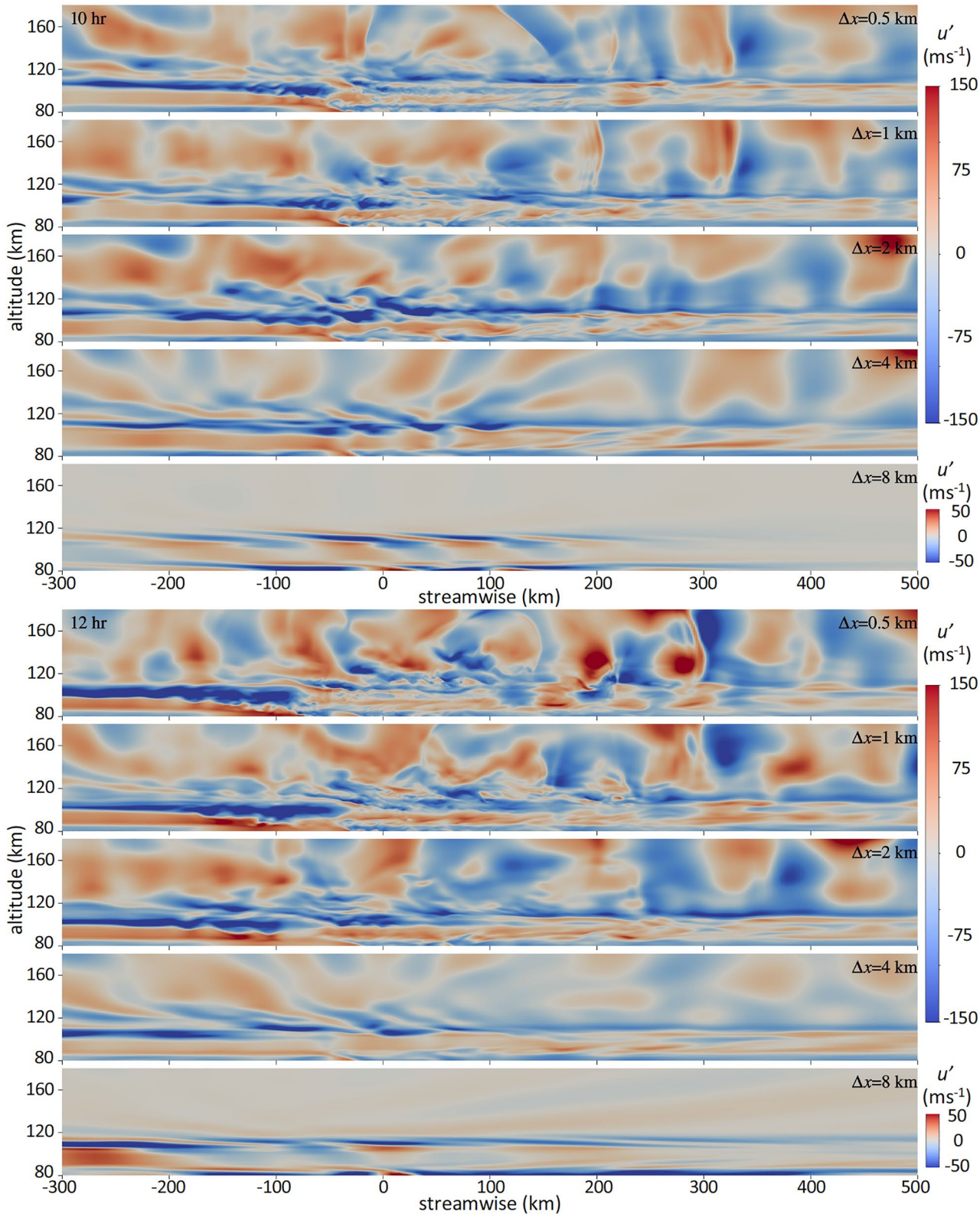

Figure 4. As in Figure 3 at 10 and 12 hr. Note the smaller color scale range for Δx = 8 km and the persistence of strong responses to late times.

Referring to Figure 3, we note the following features:

1. SGWs arise quickly in the thermosphere and persist to late times due to MW SA dynamics in the lower mesosphere,
2. SGWs rapidly penetrate to 160 km and above, and have shallower (steeper) phase slopes to the west (east) of their MW sources where intrinsic phase speeds, $c_i = c - U$, have smaller (larger) magnitudes,
3. SGW amplitudes and phases are roughly consistent for Δx = 0.5–2 km, but amplitudes decrease strongly for Δx = 4 km, are very weak for Δx = 8 km, and are delayed relative to those for Δx = 0.5–2 km at all times, as also described for SGWs at lower altitudes by F22,
4. AWs yield roughly spherical phase fronts that are reasonably well defined for Δx = 0.5 km but are rapidly degraded for coarser resolutions, and
5. AWs rapidly weaken with increasing Δx and largely disappear for Δx = 4 and 8 km, not because the AWs are not resolved, but because their amplitudes depend on resolution of MW breaking, which is very poorly described at these coarser resolutions.

The delayed and weaker responses for varying Δx were examined by F22 (see Appendix) and found to be due to a combination of under-resolved responses for smaller λ_h and phase errors induced by any finite-differencing scheme approaching the Nyquist scale. The latter induces decreasing GW phase and vertical group velocities that become large for schemes of all orders, hence are present in all finite-difference codes.

Figure 4 reveals that these dynamics persist to later times as the MW fields in the stratosphere intensify and expand downstream of, and along, the Southern Andes (see Figures 2 and 3 and the complete evolution in L20). These responses occur despite the accumulating changes in the 2-D local mean winds, ΔU that impact both (a) MW intensification, breaking, and generation of SGWs and AWs, and (b) the propagation and evolution of these secondary waves at higher altitudes; note the larger color scales in Figure 4 and see the discussion of the evolving $<\Delta U>$ in Section 5.

Figure 4 exhibits similar variations of the SGWs and AWs with coarsening resolution extending another 3 h. As at earlier times, increasing Δx causes (a) a decreasing ability to describe AW shock fronts by Δx = 2 km and their disappearance at Δx = 4 km, (b) persistence of SGWs to Δx = 2 km and their significant weakening at Δx = 4 km, and (c) failure to describe any realistic responses at Δx = 8 km.

The latter of these highlights a significant issue in modeling realistic thermospheric responses to lower atmosphere GW sources in global models having coarse resolution. While the majority of tropospheric sources are nearly linear in most cases (i.e., small initial GW amplitudes), SGW generation due to GW SA dynamics and breaking is inherently nonlinear, and their responses depend on whether these dynamics, including breaking, are adequately resolved.

4.2. $u'(x,y)$ and $w'(x,y)$ Cross Sections in the Thermosphere

We first examine the implications of decreasing resolution in $u'(x,y)$ for $\Delta x = \Delta y$ = 0.5–8 km in the thermosphere below and above the MW critical level at z = 115 km. All of these are multiple H above the primary MW breaking regions at ~50–80 km and extend from −300 to 900 km in x (400 km further east than above) and from −900 to 900 km in y with respect to the domain center between SP and NP. These are shown, respectively, at z = 100, 150, and 180 km in Figures 5–7.

The various MW and SGW responses arise in the presence of larger-scale dynamics accompanying primarily MW pseudo-momentum transport and deposition that extend from below the lowest altitudes of MW breaking in the lower mesosphere and throughout the lower thermosphere. They account for the varying larger-scale $u'(x,y)$ variations seen to intensify from 9 to 12 hr and are addressed separately in Section 5. For our discussion here, and especially at the higher altitudes, it is important to distinguish the local MW and SGW amplitudes from the local mean u', denoted ΔU in Section 5, at scales larger than the MW and SGW λ_h.

4.2.1. $u'(x,y)$ at 100 km

The $u'(x,y)$ fields at 100 km in Figure 5 reveal the smaller-scale primary MW and SGW responses much more clearly than seen in the (x,z) cross sections above. Specific features for $\Delta x = \Delta y$ = 0.5 km include the following:

1. Initial, strong, but transient, MW "bow-waves" propagate upstream of SP and NP that are stronger for the SP MW forcing,

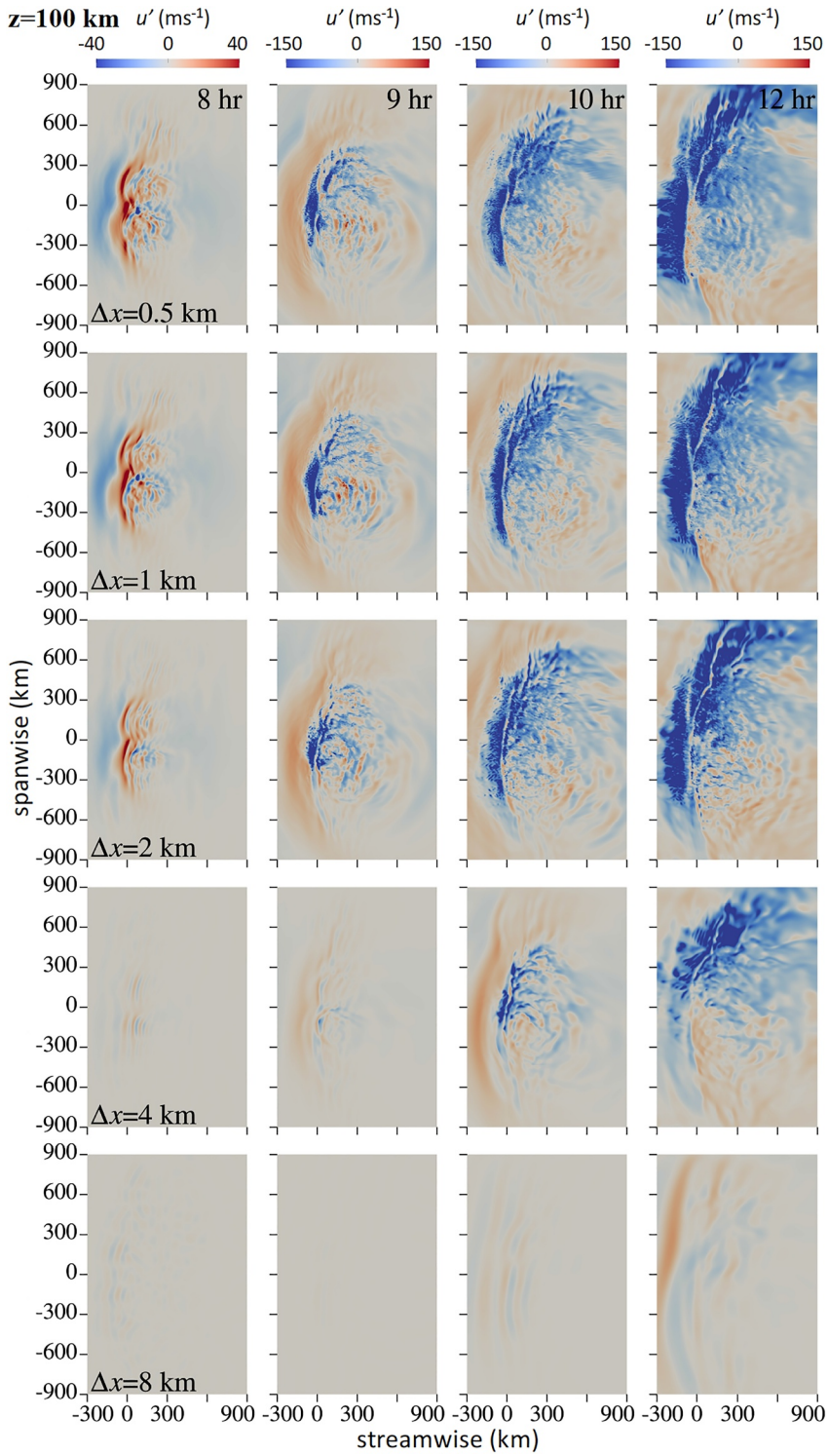

Figure 5. Horizontal cross sections, $u'(x,y)$, at z = 100 km extending 1200 (1800) km in $x(y)$ at 8, 9, 10, and 12 hr (left to right) for $\Delta x = \Delta y$ from 0.5 to 8 km (top to bottom). These show the resolved spatial scales not seen clearly in Figures 3 and 4. As above, resolution of 4 and 8 km exhibit major deficiencies relative to $\Delta x = \Delta y = 0.5$ km.

2. Larger-scale SGWs emerge by 9 hr and propagate upstream and downstream, but with smaller downstream amplitudes due to the intervening $dU/dz > 0$ above the SGW sources at lower altitudes,
3. Smaller-scale SGWs at smaller radii propagate mostly eastward at 9 hr and thereafter,

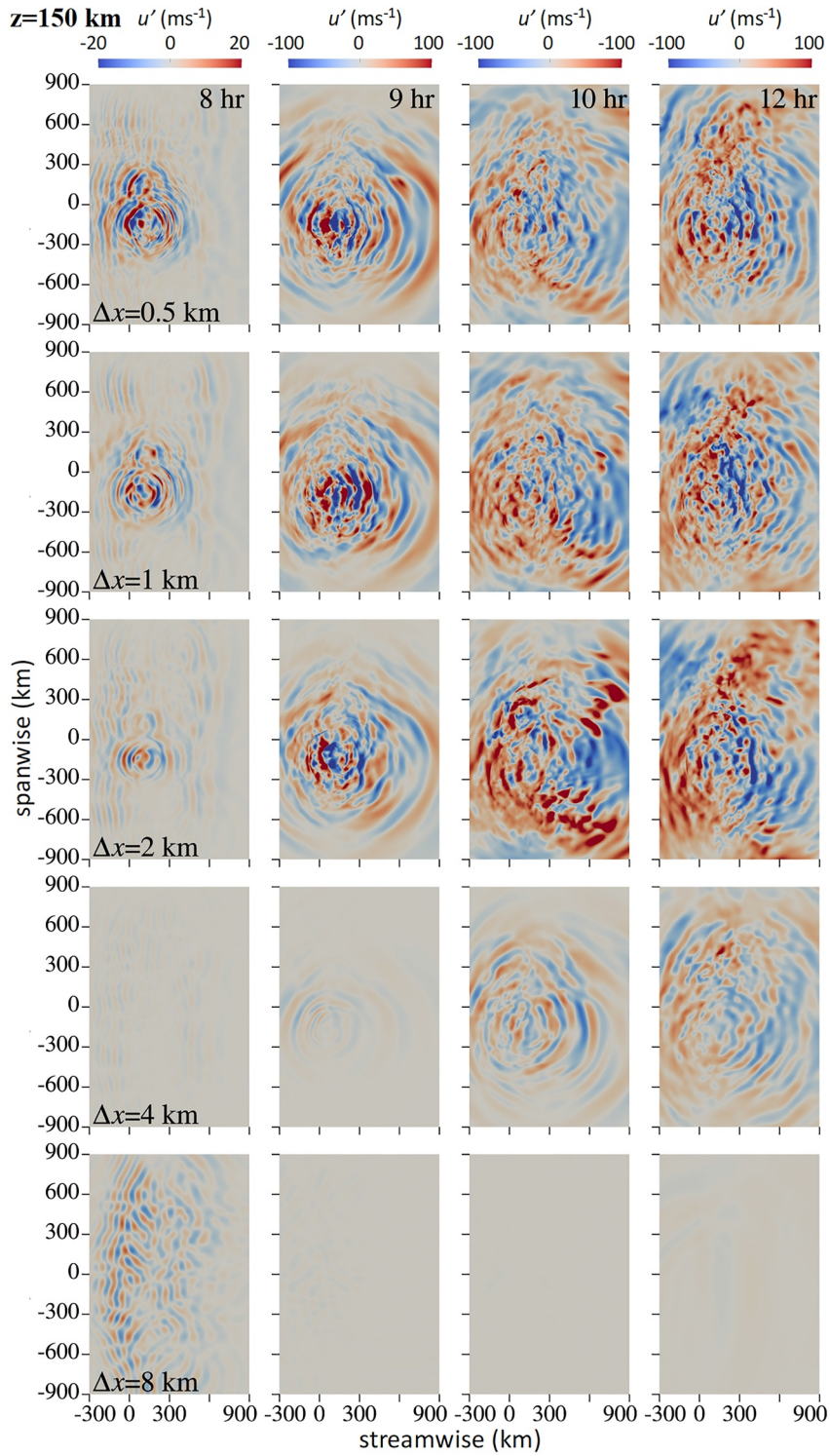

Figure 6. As in Figure 5 for $u'(x,y)$ cross sections at z = 150 km. Note the different color scales relative to Figure 5.

4. MW breaking occurs via small-scale instabilities, specifically vortex rings with diameters of ~5–10 km (see the high-resolution figures in the Supporting Information S1), and
5. A major expansion of these responses in x and y occurs by 12 hr.

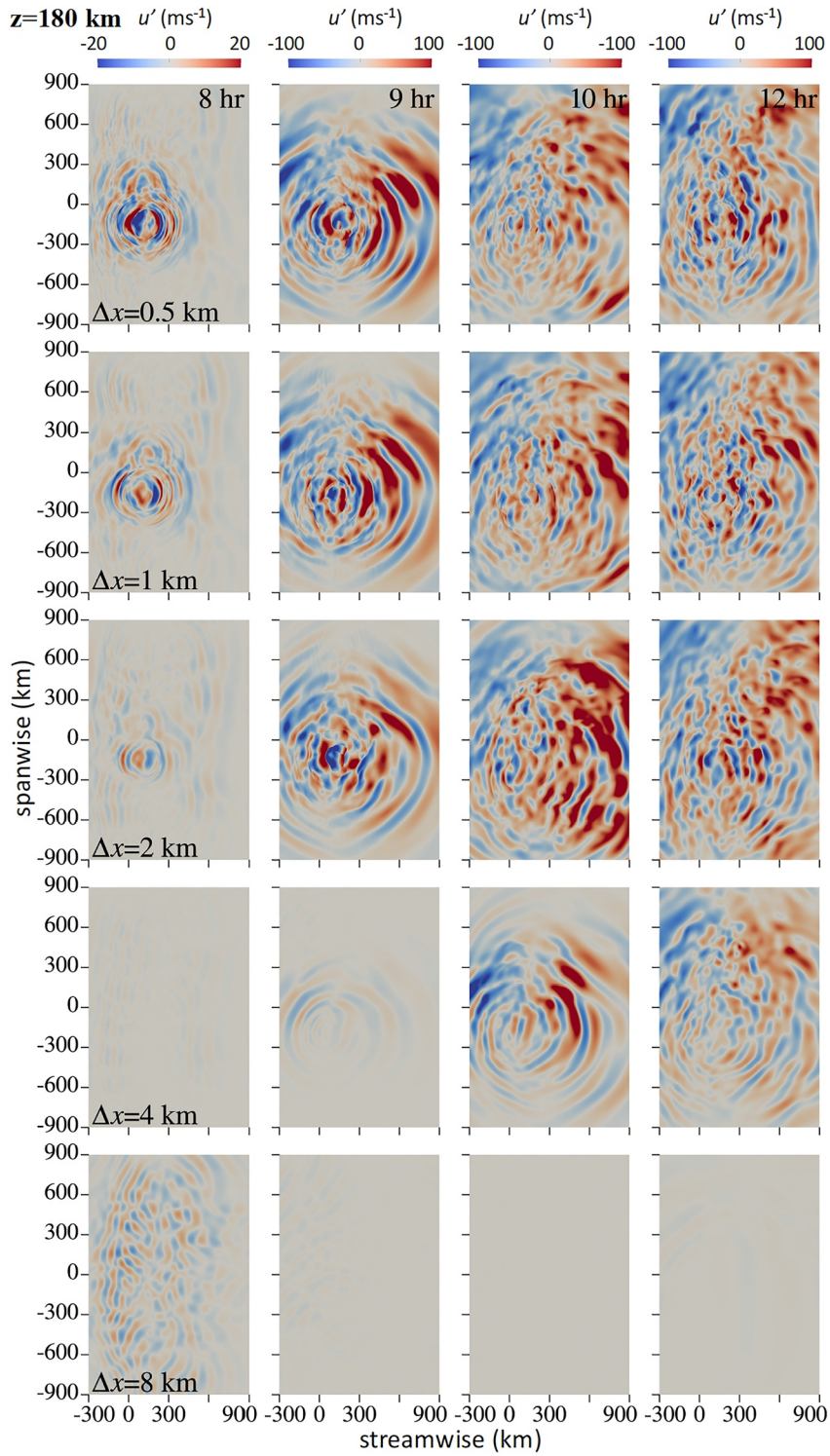

Figure 7. As in Figure 6 for $u'(x,y)$ at z = 180 km. The color scales are the same as in Figure 6 for easy comparisons.

All of the above features are impacted by decreasing resolution, but to varying degrees depending on their sources, spatial scales, and propagation environments. Those for Δx = 1 km are least impacted, with all of the features at scales of ~20 km and larger essentially unchanged, but slightly weaker. The only significant changes are seen at the smallest scales of instability dynamics due to MW breaking seen most clearly in regions of large MW

$du'/dz < 0$, where 1-km resolution cannot describe the smallest features seen for $\Delta x = 0.5$ km (see the upstream bow-wave responses and the regions with larger-scale $du'/dx < 0$ in the center-left portions of these fields).

Cross sections for $\Delta x = 2$ km are somewhat more impacted, but still closely approximate the larger-scale MW and SGW features. Specific additional deficiencies in the cross sections for $\Delta x = 2$ km relative to those for $\Delta x = 0.5$ and 1 km include the following:

1. MW "bow-wave" responses are weaker, less extensive, and less structured in x, suggesting an emerging delay relative to the responses for smaller Δx due to a reduced c_{gz}, and
2. Instabilities due to MW breaking are still described in the same regions, but occur at artificially larger, and sometimes 2-D, scales due to decreased resolution.

The $u'(x,y)$ fields for $\Delta x = 4$ km exhibit more significant departures including the following:

1. MW amplitudes and phase distortions are significantly weaker and delayed by >1 hr,
2. The peak responses are more localized and weaker than seen for $\Delta x = 0.5$–2 km, and
3. Only very weak, instability dynamics arise, and occur at artificially large scales.

The weaker and delayed responses seen for $\Delta x = 1$–4 km in Figure 5 further quantify the impacts of decreasing resolution discussed in connection with Figures 3 and 4. Specifically, they show both the clear convergence of larger- and smaller-scale features approaching $\Delta x = 0.5$ km, and the accelerated (quadratic) degradation of the solution fidelity (both resolution and character) by $\Delta x = 4$ km anticipated in the Appendix of F22 and noted above.

Lastly, the $u'(x,y)$ fields for $\Delta x = 8$ km at $z = 100$ km exhibit major departures having no resemblance to those for $\Delta x = 0.5$ km. Instead, these include a delayed response to transient forcing accounting for the field at 8 hr and significantly delayed and dramatically weaker responses to 12 hr.

4.2.2. $u'(x,y)$ at 150 km

$u'(x,y)$ fields at $z = 150$ km corresponding to those at 100 km in Figure 5 are shown in Figure 6. These fields differ from those in Figure 5 in several significant respects. They represent largely SGW responses because they are above the MW critical level at 115 km, the kinematic viscosity is sufficiently large that there are no detectable smaller-scale instability dynamics, and AWs at these altitudes have significant responses that are largely confined within ~300 km of $x = y = 0$ (i.e., the central 1/3rd of the field along y in the left half of the field along x displayed in Figure 6).

SGWs at these altitudes arise from two source types. Those having $\lambda_h \sim 50$–100 km at smaller radii are generated by strong initial MW breaking dynamics at $z \sim 50$–70 km, and below the MW critical level at later times. They have steep propagation and large c_{gz}, hence rapidly reach $z = 150$ km with initial amplitudes of $u' \sim 20$ m s^{-1} that increase to ~100 m s^{-1} within 1 hr. Those propagating toward larger x refract to larger λ_z and become less prevalent as strong breaking at lower altitudes subsides thereafter.

SGWs having $\lambda_h \sim 100$–200 km at larger radii arise primarily due to local SA dynamics initiated preceding initial MW breaking at $z \sim 50$–80 km. They also exhibit large amplitude increases due to the ~7–9 H from their source altitudes to 150 km. Due to their larger λ_h and smaller c_{gz}, however, they are seen to emerge at $z = 150$ km ~1 hr later than those having smaller λ_h and larger c_{gz}. They also persist to later times than those due to strong initial MW breaking, but become weaker and less coherent due to lessening large-scale variations in MW breaking at lower altitudes after ~8.5 hr (see F22, Figure 2, and Figure 2 above).

Also seen at small scales within ~300 km of the central response are localized, large u' gradients over very small distances that were noted above, attributed to sharp phase fronts of AWs resembling shocks by L20, and which diminish significantly after 9 hr.

Comparing the SGW fields for $\Delta x = 1$ km with those just discussed, we note very similar overall features in the central response at the same initial scales, $\lambda_h \sim 50$–100 km, but clear reductions in their extents and amplitudes relative to $\Delta x = 0.5$ km at 8 hr. These differences cannot be attributed to decreased resolution, as $\Delta x = 1$ km also easily resolves these SGW dynamics. Rather, they must instead be due to the less resolved and weaker MW

breaking dynamics at $z \sim 50$–80 km for $\Delta x = 1$ km. Thereafter, the two resolutions exhibit very similar features extending to later times, though with larger-scale, local-mean u' showing some background spatial variations.

Similar, but more significant, degradations of the SGW field occurring for $\Delta x = 0.5$ and 1 km are seen for $\Delta x = 2$ km. As for $\Delta x = 1$ km, the SGWs are easily resolved for $\Delta x = 2$ km, but the MW breaking source descriptions are further degraded (and weakened). Additionally, larger phase errors (and c_{gz} reductions) occurring for $\Delta x = 2$ km for the same SGW λ_h necessarily delay the SGW responses at higher altitudes. These cumulative influences further suppress the smaller SGW scales and amplitude at the later times.

SGWs at $z = 150$ km for $\Delta x = 4$ km exhibit very weak and non-physical responses for multiple reasons. These include the following:

1. Failure to sufficiently resolve and describe MW generation and propagation at the lowest altitudes for the smaller $\lambda_h \sim 30$–60 km, which leads to significantly reduced initial MW amplitudes, large phase errors, and reduced λ_z and c_{gz},
2. The inability to describe MW breaking dynamics driving smaller-scale SGWs, and
3. dramatically weaker SA dynamics resulting in much reduced SGW generation and responses at higher altitudes.

Together, these impacts cause the delayed and weaker SGW fields seen for $\Delta x = 4$ km in Figure 6.

Finally, the responses at $z = 150$ km for $\Delta x = 8$ km bear no resemblance to these same fields for smaller Δx because this resolution cannot resolve the initial MWs, nor their evolutions in time. That seen at 8 hr is the projection of the initial conditions at high altitudes delayed by ~8 hr due to the much reduced MW c_{gz} at this resolution, based on the estimated phase errors, and these responses weaken significantly by 9 hr. There is also a very weak, apparent large-scale SGW response seen at 12 hr that must have arisen at lower altitudes, but which has not been diagnosed due to its apparent irrelevance to the dynamics discussed above.

4.2.3. $u'(x,y)$ and $w'(x,y)$ at 180 km

The $u'(x,y)$ fields at $z = 180$ km shown in Figure 7 are remarkably similar to those at $z = 150$ km in Figure 6. They exhibit similar patterns, SGW scales and amplitudes, evolutions with time, and impacts of increasing Δx, hence we will not repeat that discussion here. The major differences are an apparent weakening of the smaller-scale SGWs at $z = 180$ km relative to $z = 150$ km due to an ~3.6 times increase in kinematic viscosity over 30 km, and apparent varying larger-scale, local-mean u' responses driven by differing pseudo-momentum flux divergence at the two altitudes. In other respects, differences are very small.

In order to more fully characterize the SGW responses at $z = 180$ km, we also show the corresponding $w'(x,y)$ fields at $z = 180$ km in Figure 8. We first consider the $w'(x,y)$ fields at 8 hr, for which the color scale range is 50% larger than that for $u'(x,y)$. The large initial w' exceeding u' implies SGWs having very high intrinsic frequencies, $\omega_i = k_h(c_h - U) \sim N/1.4$ or higher, for buoyancy frequency, N, assuming $\lambda_h << 4\pi H$, for k_h, c_h, and U the SGW horizontal wavenumber, phase speed, and mean wind in the plane of SGW propagation. In fact, SGWs seen in some regions at high altitudes in the fields shown in Figure 3 at 8 hr are apparently evanescent at the highest altitudes where $|c_h - U|$ is very large, but these do not extend to large $|x|$ and $|y|$ at this time.

As seen for $u'(x,y)$ in Figure 7, the $w'(x,y)$ fields exhibit a dramatic expansion to larger radii by 9 hr and persist to later times. But as expected, their larger amplitudes accompany smaller λ_h than dominate the $u'(x,y)$ responses at these times.

As discussed above for $u'(x,y)$, $w'(x,y)$ fields reveal the ability to reasonably approximate SGW responses at $z = 180$ km for Δx as large as 2 km. They also exhibit the same problems seen to occur for $\Delta x = 4$ and 8 km in Figure 7 for the same reasons. These are highlighted with much smaller color scales for $\Delta x = 8$ km in Figure 8. More significantly, the $w'(x,y)$ fields confirm the generation and importance of high-frequency SGWs penetrating well into the thermosphere due to MW breaking in the mesosphere.

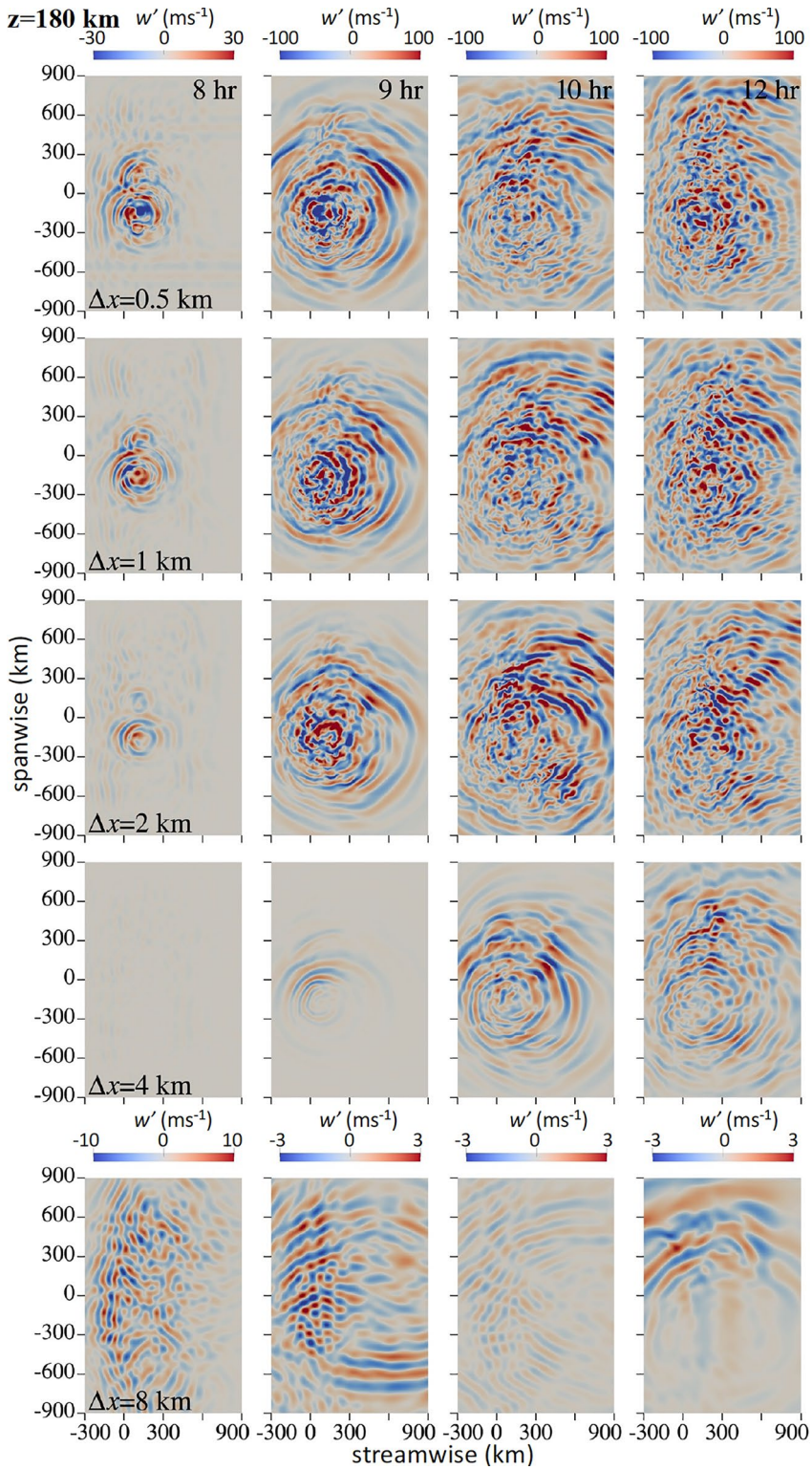

Figure 8. As in Figure 7 for $w'(x,y)$ at z = 180 km. Note the common color scales with Figure 7 at 9 hr and thereafter for Δx = 0.5–4 km.

5. Influences of Varying Resolution on MW and SGW Momentum Fluxes and Induced Mean Winds in the Thermosphere

We now describe the impacts of decreasing resolution on local mean assessments of the vertical flux of zonal momentum, denoted $<u'w'>$, and induced zonal winds accompanying full, 3-D, pseudo-momentum transport and deposition due to SGW dissipation, denoted $<\Delta U>$. Importantly, the local, 3-D nature of SGW forcing dynamics and dissipation yield induced larger-scale motions that also exhibit significant 3-D responses. Evidence of such was provided by F21, where MW and SGW propagation and dissipation for the case with Δx = 0.5 km resolution were seen to induce large local responses in $U(z)$ throughout the domain. These included $U(z)$ magnitude variations as large as 100 m s^{-1} and altitude variations of $|U|(z)$ maxima of ∼5–10 km increasing with altitude to 115 km.

The $<u'w'>$ and $<\Delta U>$ fields for varying horizontal resolution are shown in x–y planes at z = 100, 150, and 180 km in the thermosphere at which the MW and/or SGW fields are discussed above. These fields were averaged using full-width, half-maximum (FWHM) Gaussian weighting along x of 400 km at all altitudes and FWHM weighting along y of 200 km at z = 100 km, and of 400 km along y at z = 150 and 180 km, respectively. MW $<u'w'>(x,y)$ extending from −300 to 900 km along x and to ±900 km along y at z = 100, 150, and 180 km are shown at left in Figures 9–11. Corresponding $<\Delta U>(x,y)$, but extending along x to ±900 km, are shown at right in each case.

5.1. $<u'w'>(x,y)$ and $<\Delta U>(x,y)$ at 100 km

The $<u'w'>$ and $<\Delta U>$ fields for $\Delta x = \Delta y$ = 0.5 km at top in Figure 9 reveal significant emerging MW influences in the lower thermosphere accompanying initial intensification of MW breaking in the mesosphere at comparable $U \sim$ 170 m s^{-1}. This is despite a minimum $U(z) \sim$ 6 m s^{-1} at 87 km that causes major local reductions in the MW λ_z, u', $<u'w'>$, and c_{gz} at these altitudes due to critical level approach. As a result, the responses at z = 100 km are further delayed, relative to those due to the $\Delta z \sim$ 4–7 H above the initial breaking in the mesosphere. Maximum $<u'w'>$ are somewhat smaller at 100 km, occur ∼100–200 km further upstream than in the mesosphere, and are more variable in time, due to modulation of the intervening propagation environment and MW amplitudes at higher altitudes. The $<u'w'>$ maxima at 100 km span large regions along x and y, suggesting strong net drag on the eastward U and comparable larger-scale influences to those at lower altitudes. The $<u'w'>$ magnitudes and spatial extents are also very similar to those shown by F21 and F22 at z = 70 km, but are further delayed in time due to delayed MW propagation to z = 100 km.

The $<\Delta U>$ field for $\Delta x = \Delta y$ = 0.5 km at 8 hr at top right in Figure 9 resembles that at z = 50 km in F22, but at somewhat larger scales. Thereafter, it departs significantly, in large part due to influences on the $<\Delta U>$ field by larger-scale MW λ_x as they attain this altitude, and to vertical displacements of local fields, as discussed by F22. Of greater significance are the apparent "bow-wave" structure and clockwise rotation of the response viewed from above. The former is due to the localized $<u'w'>$ maximum along y from ∼8 to 10 hr; the latter can be traced to the rotation of the mean wind toward the SE at $z \sim$ 85–100 km (see Figure 1 at lower right and Figure 5).

Comparable $<u'w'>$ and $<\Delta U>$ are seen for Δx = 1 and 2 km. Those for Δx = 1 km are almost indistinguishable from those for Δx = 0.5 km; those for Δx = 1 km are slightly weaker and exhibit somewhat different $<u'w'>$ distributions along y, but are also close approximations to those fields. As noted for the $u'(x,y)$ fields at z = 100 km in Figure 5, the fields for Δx = 4 km in Figure 9 are slower to arise, significantly weaker, and relatively poor approximations of the higher-resolution fields. And as expected, based on the discussions above, and the phase errors anticipated at very coarse resolution, the fields for Δx = 8 km have very little resemblance to those at higher resolution.

5.2. $<u'w'>(x,y)$ and $<\Delta U>(x,y)$ at 150 km

The $<u'w'>$ and $<\Delta U>$ fields for $\Delta x = \Delta y$ = 0.5 km at z = 150 km at top in Figure 10 differ in significant respects from those in Figure 9 because they reflect primarily SGW influences without MW contributions, due to the MW critical level at z = 115 km. Given the discussion of Figure 7 above, we expect SGW negative (positive) $<u'w'>$ westward (eastward) of the major SGW responses centered east of the Andes throughout the evolution.

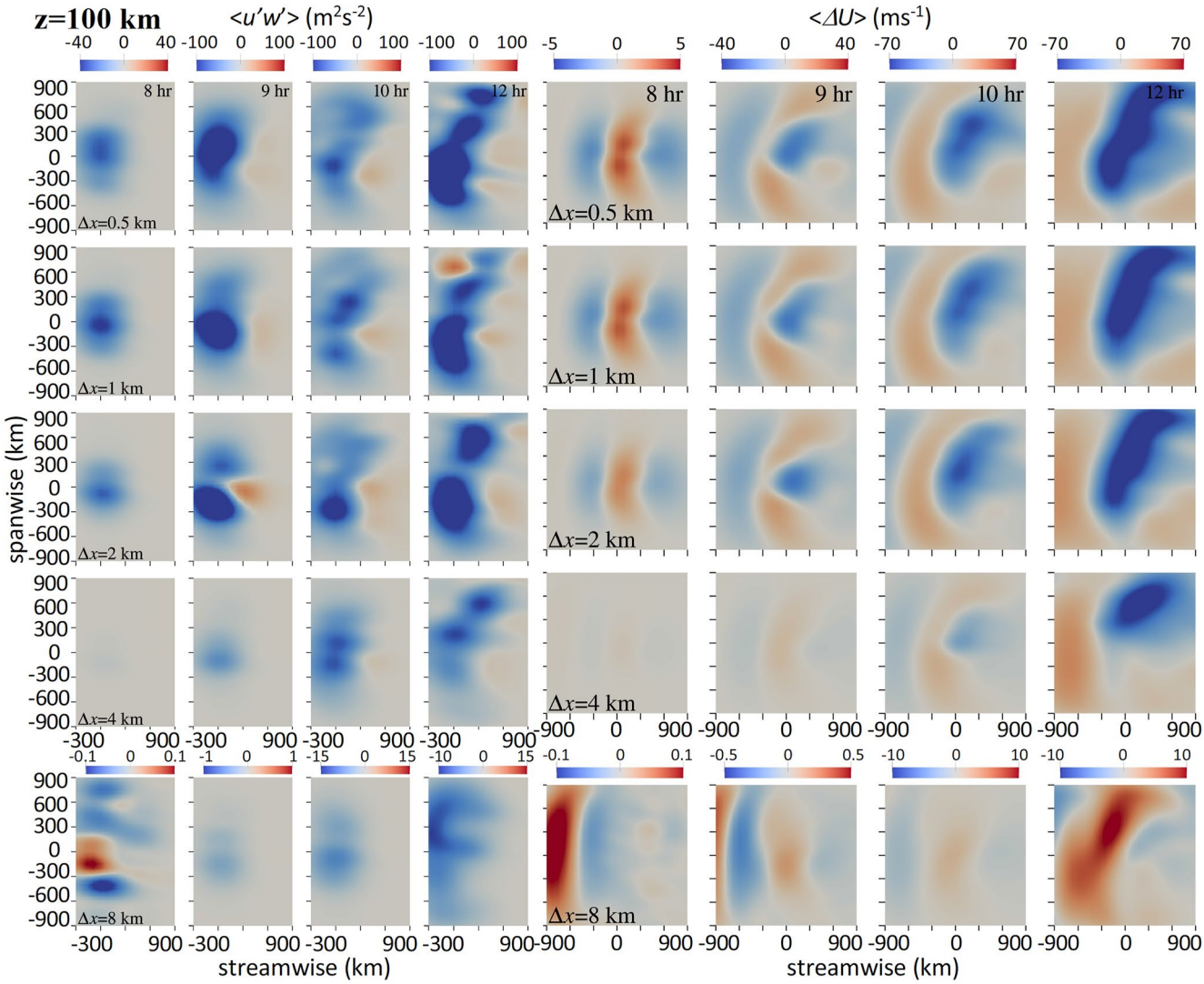

Figure 9. $\langle u'w' \rangle(x,y)$ and $\langle \Delta U \rangle(x,y)$ (left and right panel sets), at z = 100 km extending 1200 (1800) km in $x(y)$ at 8, 9, 10, and 12 hr (left to right in each panel set) for $\Delta x = \Delta y$ from 0.5 to 8 km (top to bottom). These fields employed Gaussian weighting as described in the text.

This is largely reflected in the fields at top left, though with variations in the orientations of the larger $\langle u'w' \rangle$ gradients with time.

Cumulative $\langle u'w' \rangle(x,y)$ at z = 150 km quickly become dramatically larger than seen accompanying MWs in the mesosphere or at z = 100 km in Figure 9. These drive very different $\langle \Delta U \rangle(x,y)$ than seen due to MW forcing at the same altitudes. In this case, SGW $\langle u'w' \rangle$ gradients, and the more complete pseudo-momentum fluxes drive divergent zonal motions centered over NP and SP. However, the responses are advected to the SSW at ~80–90 m s^{-1}, and only the intensifying eastward $\langle \Delta U \rangle$ is seen emerging at the later times at upper right in Figure 10 for Δx = 0.5 km.

Unlike the MW responses at z = 100 km discussed above, both the $\langle u'w' \rangle$ and $\langle \Delta U \rangle$ SGW fields at z = 150 km also intensify significantly by 9 and 10 hr for Δx = 1 and 2 km, respectively, relative to those for Δx = 0.5 km. For the case with Δx = 2 km, the $\langle \Delta U \rangle$ responses are larger and more extended spatially than those for higher resolution. The causes of these differing responses are likely complex and have not been diagnosed. However, we note that the spectra discussed in Section 6 for these smaller Δx exhibit very different responses at SGW λ_x ~ 40–100 km most likely to be generated by MW breaking dynamics below.

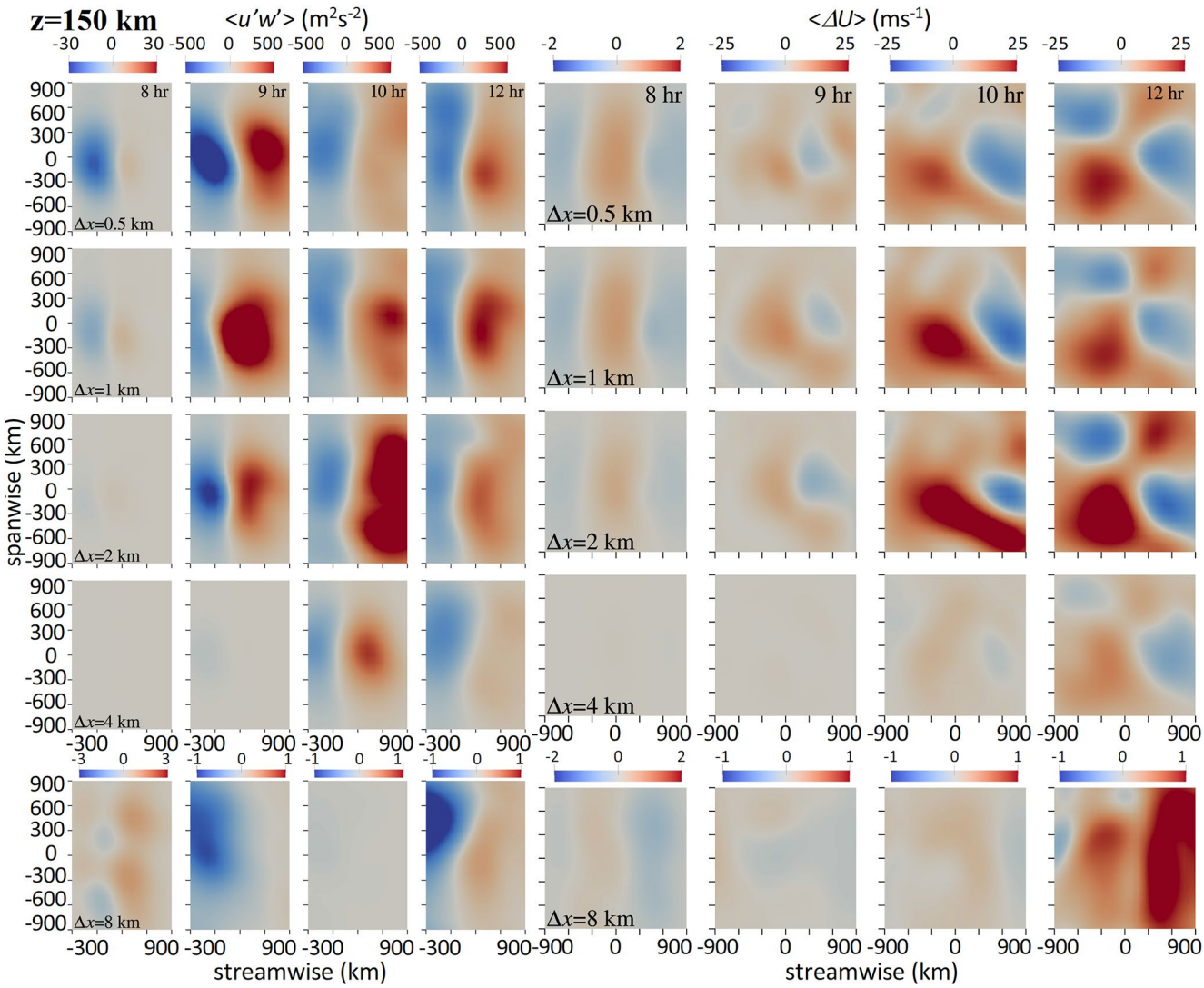

Figure 10. As in Figure 9 for $<u'w'>(x,y)$ and $<\Delta U>(x,y)$ at z = 150 km.

By comparison, both $<u'w'>$ and $<\Delta U>$ for Δx = 4 km reveal only very weak responses at 8 and 9 hr, but have similar, though much weaker, features at 10 and 12 hr. As above, the responses for Δx = 8 km are almost non-existent.

5.3. $<u'w'>(x,y)$ and $<\Delta U>(x,y)$ at 180 km

Responses in the $<u'w'>$ fields for $\Delta x = \Delta y$ = 0.5 km at z = 180 km at top left in Figure 11 closely resemble those at 150 km in Figure 10. As at the lower altitude, these reveal divergent forcing along x away from the major SGW sources in the lee of SP and NP. These fields are a result of the outward, and largely zonal, SGW propagation seen in Figures 7 and 8, especially toward E, given the predominance of eastward-propagating SGWs at these times. The corresponding induced $<\Delta U>$ are seen to be displaced increasingly northward with time relative to the peak $<u'w'>$. This is consistent with the mean winds at this altitude that exhibit largely northward advection at $V \sim$ 25–30 m s^{-1} at this altitude in the absence of strong local forcing at earlier times (see Figure 1).

The corresponding responses for Δx = 1 km agree closely with those at Δx = 0.5 km, and that for Δx = 2 km is weaker to ~9 hr, but comparable or stronger thereafter. As above, the responses for Δx = 4 and 8 km are very weak or largely absent by comparison.

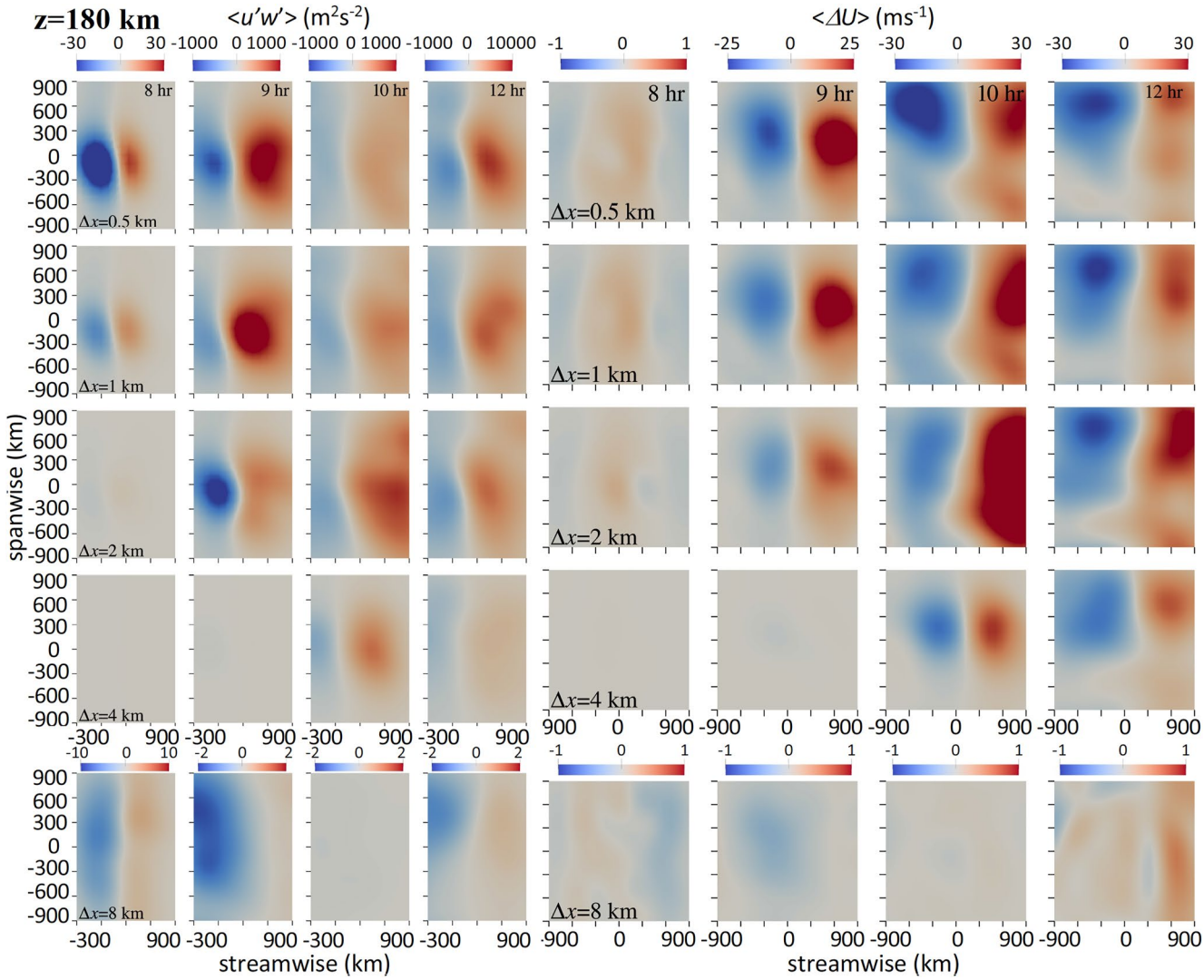

Figure 11. As in Figures 9 and 10 for $<u'w'>(x,y)$ and $<\Delta U>(x,y)$ at $z = 180$ km.

6. $<u'w'>$ Spectra Over NP and SP

MW and SGW $<u'w'>$ streamwise spectra over NP and SP computed along the full computational domain and averaged over ±25 km in y are shown in Figure 12. Those at left (right) are averaged from 8 to 9 (10–12) hr; the upper, middle, and lower 4-panel sets are for altitudes of 100, 150, and 180 km, respectively; those at top (bottom) in each 4-panel set are along x over NP (SP). MF spectra in these same forms at 50 and 70 km were discussed by F22. Those exhibited almost exclusively MW responses because SGWs generated by strong breaking as low as 50 km did not acquire sufficiently large amplitudes to compete with MW amplitudes only 20 km above.

A summary of the spectral features for $\Delta x = 0.5$ km described by F22 includes the following:

1. Initial peak negative $<u'w'>$ at MW $\lambda_x \sim 40$–80 km at 50 and 70 km,
2. Evidence of transient evanescence at $\lambda_x \sim 30$–40 km at $z = 50$ km due to the very large $U \sim 190$ m s^{-1} over SP and NP at earlier and later times, respectively,
3. Increasing negative MW $<u'w'>$ to $\lambda_x > 100$ km as they attain higher altitudes after 9 hr, and
4. Small, positive $<u'w'>$ due to MW instabilities at small scales where $dU/dz < 0$.

The $<u'w'>$ spectra at $z = 100$ km at top in Figure 12 exhibit significantly greater variability than those at 50 and 70 km described by F22. $u(x,z)$ fields at top in Figure 2 show the spectral contributions to also occur over a much

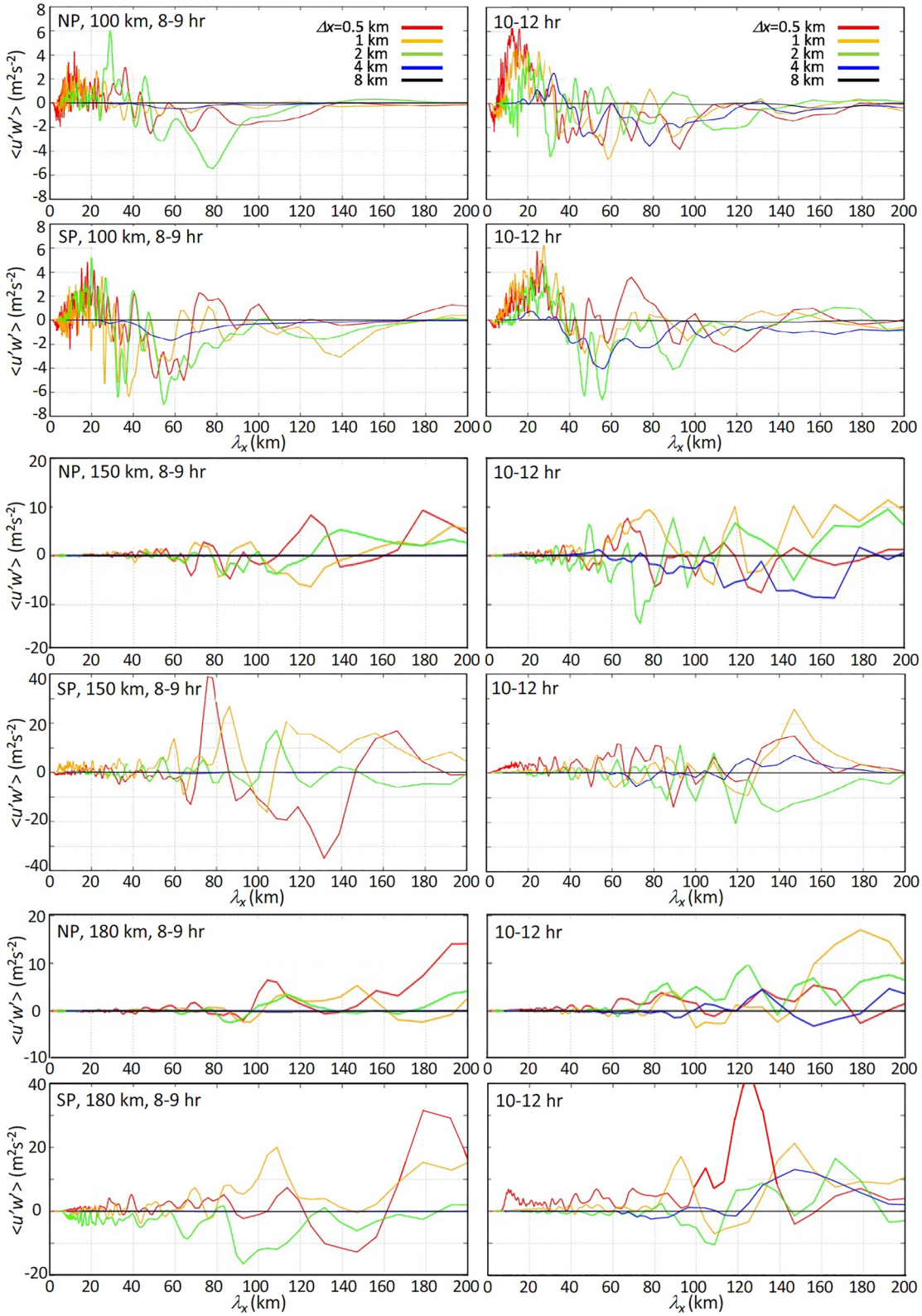

Figure 12. MW and SGW spectra showing mean $<u'w'>(\lambda_x)$, which under-estimate peak $<u'w'>$ when both positive and negative values contribute. The spectra are averaged horizontally using the Gaussian weighting as described in the text. Color codes for the various Δx are shown at top.

larger streamwise extent than at lower altitudes. These features suggest that the spectral amplitudes at any λ_x likely include contributions from both MWs and SGWs in different regions, and thus are likely significant under-estimates of the mean positive or negative $<u'w'>(\lambda_x)$ in any specific portion of the streamwise motion field.

Despite the expected superpositions of MW and SGW responses, some insightful inferences can be drawn. The spectra at $z = 100$ km for $\Delta x = 0.5$ km somewhat resemble those at 50 and 70 km described by F22 whereas those at 150 and 180 km do not. Mean $<u'w'>$ at $z = 100$ km averaged over the dominant MW λ_x noted at lower altitudes yield a negative mean at $\lambda_x \sim 40$–70 km, as seen over SP at both altitudes and averaging intervals. In contrast, mean $<u'w'>$ at $\lambda_x \sim 70$–90 km is positive and contributed by SGWs at $x \sim 100$–400 km based on the upper panels of Figure 2 showing SGWs propagating eastward, as discussed by F22. Variable mean $<u'w'>$ at $\lambda_x \sim 150$ km and larger are almost certainly SGW responses, given their absence at lower altitudes and sometime positive values. Finally, clear smaller-scale responses at $z = 100$ km arise from two primary sources:

1. Small-scale SGWs are excited by small-λ_z MW breaking due to decreasing $c_i \sim -U$ below the $U(z)$ minimum at $z = 87$ km and have primarily $c > U$ and positive $<u'w'>$, and
2. Instability dynamics due to larger-scale MW breaking at $z = 100$ km where $U \sim 170$ m s^{-1} are seen for smaller Δx in the $u'(x,y)$ cross sections at top in Figure 5.

Turning to the $<u'w'>$ spectra at $z = 150$ and 180 km at center and bottom in Figure 12, we see no significant contributions at very small scales, in sharp contrast to the spectra at $z = 100$ km and below. This is because GWs at 150 km and above are strongly impacted by very large kinematic viscosity that prevents any small-scale instability dynamics, independent of the GW amplitudes. The small-scale $<u'w'>$ at these altitudes are instead artifacts of the imperfect CGCAM resolution of AW shock fronts seen to exhibit coherence over small distances along the fronts at very small, resolved scales at smaller x and y at top in Figures 6 and 7.

The $<u'w'>$ spectra at $z = 150$ and 180 km are dominated by SGWs largely propagating in E-W directions over SP and NP, with $\lambda_x \sim 70$–200 km and $\lambda_z \sim 50$ km and larger, based on the x-z and x-y cross sections in Figures 3–8. SGW $<u'w'>$ spectral amplitudes achieve magnitudes up to ∼5 times larger than seen at $z = 100$ km. However, the true $<u'w'>$ for individual portions of the larger-scale SGW fields are very much larger, given that observed u' maxima are ∼100 m s^{-1} or larger (Figures 3–7), w' at these λ_x are smaller than u' by factors of only ∼2–3 (see L20, Figures 4 and 11), and the eastward- and westward-propagating SGW fields have similar λ_x (e.g., $<u'w'> \sim 1000$ m^2 s^{-2} or larger averaged over a single SGW λ_x), so necessarily lead to significant reductions in averaged $<u'w'>(\lambda_x)$ spectral ranges. The large variations in $<u'w'>(\lambda_x)$ amplitudes for $\Delta x = 0.5$, 1, and 2 km thus reveal variations due to SGW source sensitivity rather than to the limited resolution of the relevant λ_x. Spectral responses for $\Delta x = 4$ km further under-estimate and mis-represent $<u'w'>$ relative to smaller MW and SGW amplitudes for the same reasons; those for $\Delta x = 8$ km are essentially zero. Large phase errors at $\Delta x = 4$ and 8 km further reduce these responses.

7. Implications for Global Modeling of Gravity Wave Dynamics and Responses

F22 addressed the relations of our multi-resolution CGCAM MW simulations to previous efforts assessing resolution capabilities and implications for GW dynamics and larger-scale responses arising from MW and convective GW (CGW) generation in the troposphere. This literature is broad, diverse, and expanding rapidly, given its relevance to weather and climate prediction. In contrast, no studies to date have explored the resolution required to adequately describe thermospheric GW responses arising from tropospheric sources of direct relevance to coupled thermosphere-ionosphere dynamics and Space Weather (SW) forecasting and applications.

There are now multiple middle and whole atmosphere global models that extend into the lower thermosphere (∼140–200 km) or to the exobase (∼400–700 km) that address neutral atmosphere-ionosphere responses to neutral dynamics at lower altitudes. They perform simulations at "moderate" (∼200 km) and "enhanced" (25–100 km) horizontal resolutions employing parameterizations of sub-grid-scale GW physics. Examples with which we are most familiar include the NCAR Whole Atmosphere Community Climate Model (WACCM; Liu et al., 2014; Richter et al., 2010) and its upward extension into the ionosphere (WACCM-X; Liu et al., 2018, 2019), the U.S. Naval Research Laboratory NAVy Global Environment Model employing advanced data assimilation (NAVGEM; Satterfield et al., 2022), and the NOAA and University of Colorado Whole Atmosphere Model (WAM). Others relevant to this study are the Kühlungsborn Mechanistic general Circulation Model addressing

SGWs in the thermosphere (KMCM; Becker & Vadas, 2018; Vadas & Becker, 2019), its high-altitude extension to ∼450 km (i.e., HIAMCM; Becker & Vadas, 2020), the German ICON general circulation model (GCM; Crueger et al., 2018; Giorgetta et al., 2018) enabling high-resolution regional nesting, the UA-ICON ionospheric extension (Borchert et al., 2019), the Japanese Ground-to-Topside Model of the Atmosphere and Ionosphere for Aeronomy (GAIA; Sato et al., 2018; Yasui et al., 2018), and the Japanese Atmospheric GCM for Upper Atmosphere Research (JAGUAR; Watanabe et al., 2015).

WACCM, employing ∼25-km resolution and hydrostatic dynamics, was able to describe large-scale (λ_h > 150–200 km) MWs in northern winter over the Rockies and Tibet, and CGWs extending to ∼100 km over much larger regions (Liu et al., 2014). These GWs were able to reverse the summer mesospheric wind due to parameterized dissipation and pseudo-momentum deposition, but only decreased the winter mesospheric wind, due to $<u_h'w'>$ constrained by artificially weak maximum $|w'| \sim |u_h'|/10 \sim 7$ m s^{-1} and corresponding fluxes at $z \sim 100$ km, due to coarse resolution. WACCM-X extends to ∼700 km and includes descriptions of neutral dynamics and electrodynamics, and ion chemistry and transport, at much coarser resolution, but nevertheless captures multiple large-scale neutral and plasma dynamics and features observed in the thermosphere (Liu et al., 2018).

HIAMCM includes non-hydrostatic dynamics and ion drag in order to address GW dynamics and tidal influences. It accounts for GW λ_h as small as ∼165 km, and captures multiple aspects of GW-tidal interactions and mean responses extending into the thermosphere. It also describes SGW generation via parameterized dissipation at lower altitudes.

Neither NAVGEM nor WAM were employed for studies of GW dynamics in the thermosphere to date. KMCM, employing hydrostatic dynamics and spectral resolution describing GW λ_h > 165 km (comparable to WACCM) in a domain extending to 135 km, was used by Vadas and Becker (2019) to study SGW generation in the MLT. HIAMCM (Becker & Vadas, 2020) describing non-hydrostatic dynamics extends these capabilities to much higher altitudes. KMCM, HIAMCM, WACCM, and WACCM-X resolutions enable SGW generation due to large-scale body forcing accompanying nonlinear interactions among large-scale GWs having their amplitudes constrained by parameterization of dissipation due to smaller-scale, unresolved instability dynamics at lower altitudes. However, these model resolutions currently preclude descriptions of much stronger body forcing of SGWs by small-scale GW packets, and their SA dynamics, often occurring on spatial scales of ∼70–200 km in the thermosphere accompanying high-resolution modeling (e.g., Dong et al., 2020, 2021; Fritts et al., 2020; L20) and seen for smaller Δx in Figures 6–8.

Studies employing the enhanced (∼110 km) horizontal resolution of the GAIA whole atmosphere model having a MW parameterization (Yasui et al., 2018) revealed regions of GW Eliassen-Palm pseudo-momentum flux divergence due to resolved GWs in the MLT to be competitive with those due to parameterized GWs in all seasons, despite coarse GAIA (T106L150, ∼1.1°) resolution. In contrast to those seen in KMCM discussed above (Vadas & Becker, 2019), those in GAIA were attributed to GW radiation from unstable shears in the MLT. Importantly, these dynamics depend strongly on the larger-scale dynamics driving shear formation, and these are constrained by GAIA resolution and parameterized physics in the MLT. A study of vertical resolution influences by Watanabe et al. (2015) using JAGUAR focusing on altitudes below 80 km revealed the need for enhanced vertical resolution to account for GW momentum fluxes, even for inertia-GWs having large λ_h, where GW λ_z decreases significantly in close proximity to a critical level.

Our results discussed here and by F22 will hopefully prove beneficial in guiding developments and evaluations of new parameterizations of these various dynamics in middle and whole atmosphere GCMs. One example that is clearly of major importance is SGW generation, given its demonstrated roles in KMCM, despite coarse resolution, and regional models revealing these dynamics to arise easily and naturally for localized GWs (Dong et al., 2020, 2021; Fritts et al., 2020; L20, F21). Initial approximations to SGW generation due to 3-D body forcing (i.e., Luo & Fritts, 1993; Vadas & Fritts, 2001, 2002; Vadas et al., 2003) were based on linear theory that captures an important element of these dynamics, specifically forcing by induced local mean winds. However, linear theory fails entirely to account for "back" influences of local body forcing of the local GW field due to "self-acceleration" (SA) dynamics noted above, including those accompanying GW breaking. Such parameterization efforts could employ both high- and low-resolution versions of CGCAM and other high-resolution models, in order to resolve, and guide approximations to, initial SA dynamics and SGW responses.

One area in which guidance can be inferred from the fields described above is in the expected SGW amplitudes, scales, and MFs that accompany strong SA dynamics and breaking at lower altitudes. While the various cross sections and spectra discussed above reveal the typical scales and amplitudes of the SGW responses, they do not specifically quantify their typical pseudo-momentum fluxes locally, nor by averaging along the streamwise domain. Approximations to these MFs are provided by the averaged $<u'w'>$ estimates in Figures 9–11, and for individual SGWs as $u_h'w'/2$. The $<u'w'>$ fields for $\Delta x = \Delta y = 0.5$, 1, and 2 km exhibit peak magnitudes significantly exceeding 100, 500, and 1000 $m^2\ s^{-2}$ at 100, 150, and 180 km. However, larger $|u_h'w'|/2$ for individual SGWs are obtained for assessments, assuming $|w'|$ comparable to or exceeding $|u_h'|$, for individual SGW peak $u_h' \sim 100$ m s^{-1} at 150–180 km. This yields individual SGW estimates as large as $|u_h'w'|/2 \sim 5000$ $m^2\ s^{-2}$ at 150–180 km accompanying intense SGW forcing at lower altitudes. For reference, previous estimates employing OH airglow and related instrumentation yielded estimates as large as ~600–900 $m^2\ s^{-2}$ at $z \sim 85$–90 km (Fritts et al., 2002, 2014; Taylor et al., 2019), with larger magnitudes implied for larger scales at higher altitudes.

8. Conclusions

CGCAM simulations of MW and SGW dynamics over the Southern Andes extending into the lower thermosphere for horizontal resolutions varying from 0.5 to 8 km were described and inter-compared above. Key findings among these include the following:

1. MWs attain large amplitudes and instability scales to $z \sim 100$ km due to a secondary $U(z)$ maximum that are described well for $\Delta x = 0.5$ and 1 km, but that are delayed and weakened for $\Delta x = 2$ km, largely absent for $\Delta x = 4$ km, and badly mis-represented for $\Delta x = 8$ km,
2. SGWs dominate the responses at $z = 150$ and 180 km, have larger $\lambda_h \sim 100$–200 km at earlier times due to resolved MW breaking in the mesosphere, and weaker responses at $\lambda_h \sim 70$–150 km apparently arising largely from MW breaking at $z \sim 100$ km at later times,
3. Coarsening resolution has major impacts on the SGW amplitudes and $<u'w'>$ spectra, altering the contributing λ_h and weakening spectral amplitudes and larger-scale responses due to weakened SGWs sources in less well resolved MW breaking regions, and
4. SGWs at $\lambda_h \sim 100$–200 km have comparable amplitudes in u' and w', hence very high ω_i, and a potential for rapid forcing of the lower thermosphere, and perhaps higher altitudes.

Implications for GCMs addressing thermospheric GWs due to small-scale tropospheric sources are that (a) current resolution is much too coarse to enable realistic primary GWs and SGWs in the thermosphere, (b) the major SGW sources are GW SA and breaking dynamics that are nonlinear, unresolved, and cannot be approximated by linear theory, (c) the major SGW λ_h, $<u_h'w'>$, and thermospheric forcing occur for $\lambda_h \sim 100$–200 km that are now largely unresolved, and (d) GWs having larger λ_h exhibit the same instability scales for common λ_z, hence yield similar SGW responses. AWs, in contrast, appear to play minimal roles in MLT dynamics due to their high phase speeds and minimal dissipation, apart from their presence confirming nominal resolution of the primary MW breaking dynamics in the upper stratosphere and lower mesosphere.

Data Availability Statement

Supplemental Materials include high-resolution figures and https://zenodo.org/deposit/5823428 hosts the figures and the data files needed to recreate the figures.

Acknowledgments
Research described here was performed under AFOSR grant FA9550-18-0009, NASA awards 80GSFC18C0007 and 80NSSC20K0170, and NSF grants AGS-1647354, and AGS-2131350 cited in GEMS. We thank the DoD HPCMP for access to computational resources that enabled this modeling study. Contributions by VY were supported by the NASA/GSFC Cooperative Agreement 80NSSC21M0180 to Catholic University of America. We also thank two anonymous reviewers for multiple comments that improved the paper.

References

Artru, J., Ducic, V., Kanamori, H., Lognonne, P., & Murakami, M. (2005). Ionospheric detection of gravity waves induced by Tsunamis. *Geophysical Journal International*, *160*(3), 840–848. https://doi.org/10.1111/j.1365-246x.2005.02552.x

Azeem, I., Yue, J., Hoffmann, L., Miller, S. D., Straka, W. C., III, & Crowley, G. (2015). Multisensor profiling of a concentric gravity wave event propagating from the troposphere to the ionosphere. *Geophysical Research Letters*, *42*, 7874–7880. https://doi.org/10.1002/2015GL065903

Becker, E., & Vadas, S. L. (2018). Secondary gravity waves in the winter mesosphere: Results from a high-resolution global circulation model, *Geophysical Research Letters*, *123*, 2605–2627. https://doi.org/10.1002/2017JD027460

Becker, E., & Vadas, S. L. (2020). Explicit global simulation of gravity waves in the thermosphere. *Journal of Geophysical Research—A: Space Physics*, *125*, e2020JA028034. https://doi.org/10.1029/2020JA028034

Borchert, S., Zhou, G., Baldauf, M., Schmidt, H., Zängl, G., & Reinert, D. (2019). The upper-atmosphere extension of the ICON general circulation model (version: Ua-icon-1.0), *Geoscientific Model Development*, *12*, 3541–3569. https://doi.org/10.5194/gmd-12-3541-2019

Crueger, T., Giorgetta, M. A., Brokopf, R., Esch, M., Fiedler, S., Hohenegger, C., et al. (2018). ICON-A, the atmosphere component of the ICON Earth system model: II. Model evaluation, *Journal of Advances in Modeling Earth Systems*, *10*, 1638–1662. https://doi.org/10.1029/2017MS001233

de Wit, R. J., Janches, D., Fritts, D. C., Stockwell, R. G., & Coy, L. (2017). Unexpected climatological behavior of MLT gravity wave momentum flux in the lee of the Southern Andes hot spot. *Geophysical Research Letters*, *44*, 1182–1191. https://doi.org/10.1002/2016GL072311

Djuth, F. T., Sulzer, M. P., Gonzales, S. A., Mathews, J. D., Elder, J. H., & Walterscheid, R. L. (2004). A continuum of gravity waves in the Arecibo thermosphere? *Geophysical Research Letters*, *31*, L16801. https://doi.org/10.1029/2003GL019376

Dong, W., Fritts, D. C., Lund, T. S., Wieland, S. A., & Zhang, S. (2020). Self-acceleration and instability of gravity wave packets: 2. Two-dimensional packet propagation, instability dynamics, and transient flow responses. *Journal of Geophysical Research: Atmospheres*, *125*, e2019JD030691. https://doi.org/10.1029/2019JD030691

Dong, W., Fritts, D. C., Thomas, G. E., & Lund, T. S. (2021). Modeling responses of polar mesospheric clouds to gravity wave and instability dynamics and induced large-scale motions. *Journal of Geophysical Research: Atmospheres*, *126*, e2021JD034643. https://doi.org/10.1029/2021JD034643

Fritts, D. C., Dong, W., Lund, T. S., Wieland, S., & Laughman, B. (2020). Self-acceleration and instability of gravity wave packets: 3. Three-dimensional packet propagation, secondary gravity waves, momentum transport, and transient mean forcing in tidal winds, *Journal of Geophysical Research: Atmospheres*, *125*, e2019JD030692. https://doi.org/10.1029/2019JD030692

Fritts, D. C., Laughman, B., Lund, T. S., & Snively, J. B. (2015). Self-acceleration and instability of gravity wave packets: 1. Effects of temporal localization. *Journal of Geophysical Research: Atmospheres*, *120*, 8783–8803. https://doi.org/10.1002/2015JD023363

Fritts, D. C., Lund, T. S., Lund, A. C., & Yudin, V. (2022). Impacts of limited model resolution on the representation of mountain wave and secondary gravity wave dynamics in local and global models, Part 1: Mountain waves in the stratosphere and mesosphere. Accepted.

Fritts, D. C., Lund, T. S., Wan, K., & Liu, H.-L. (2021). Numerical simulation of mountain waves over the southern Andes, Part 2: Momentum fluxes, mean-flow accelerations, and gravity-wave/tidal interactions. *Journal of the Atmospheric Sciences*, *78*, 3069–3088. https://doi.org/10.1175/JAS-D-20-0207.1

Fritts, D. C., Pautet, P.-D., Bossert, K., Taylor, M. J., Williams, B. P., Iimura, H., et al. (2014). Quantifying gravity wave momentum fluxes with Mesosphere Temperature Mappers and correlative instrumentation. *Journal of Geophysical Research-Atmospheres*, *119*, 13583–13603. https://doi.org/10.1002/2014JD022150

Fritts, D. C., Vadas, S. A., & Yamada, Y. (2002). An estimate of strong local gravity wave body forcing based on OH airglow and meteor radar observations, *Geophysical Research Letters*, *29*(10), 1429. https://doi.org/10.1029/2001gl013753

Galvan, D. A., Komjathy, A., Hickey, M. P., Stephens, P., Snively, J., Tony Song, Y., et al. (2012). Ionospheric signatures of Tohoku-Oki tsunami of March 11, 2011: Model comparisons near the epicenter. *Radio Science*, *47*, RS4003. https://doi.org/10.1029/2012RS005023

Giorgetta, M. A., Brokopf, R., Crueger, T., Esch, M., Fiedler, S., Helmert, J., et al. (2018). ICON-A, the atmosphere component of the ICON Earth system model: I. Model description, *Journal of Advances in Modeling Earth Systems*, *10*, 1613–1637. https://doi.org/10.1029/2017MS001242

Godin, O. A., Zabotin, N. A., & Bullett, T. W. (2015). Acoustic-gravity waves in the atmosphere generated by infragravity waves in the ocean. *Earth Planets and Space*, *67*, 47. https://doi.org/10.1186/s40623-015-0212-4

Heale, C. J., Lund, T., & Fritts, D. C. (2020). Convectively generated gravity waves during solstice and equinox conditions. *Journal of Geophysical Research: Atmospheres*, *125*, e2019JD031582. https://doi.org/10.1029/2019JD031582

Hines, C. O. (1960). Internal atmospheric gravity waves at ionospheric heights, *Canadian Journal of Physics*, *38*, 1441–1481. https://doi.org/10.1139/p60-150

Komjathy, A., Galvan, D. A., Stephens, P., Butala, M. D., Akopian, V., Wilson, B., et al. (2012). Detecting ionospheric TEC perturbations caused by natural hazards using a global network of GPS receivers: The Tohoku case study. *Earth Planets and Space*, *64*, 1287–1294. https://doi.org/10.5047/eps.2012.08.003

Laughman, B., Fritts, D. C., & Lund, T. S. (2017). Tsunami-driven gravity waves in the presence of vertically varying background and tidal wind structures. *Journal of Geophysical Research-Atmospheres*, *122*, 5076–5096. https://doi.org/10.1002/2016JD025673

Liu, H.-L. (2019). Quantifying gravity wave forcing using scale-invariance. *Nature Communications*, *10*, 2605. https://doi.org/10.1038/s41467-019-10527-z

Liu, H.-L., Bardeen, C. G., Foster, B. T., Lauritzen, P., Liu, J., Lu, G., et al. (2018). Development and validation of the whole atmosphere community climate model with thermosphere and ionosphere extension (WACCM-X 2.0). *Journal of Advances in Modeling Earth Systems*, *10*, 381–402. https://doi.org/10.1002/2017ms001232

Liu, H.-L., McInerney, J. M., Santos, S., Lauritzen, P. H., Taylor, M. A., & Pedatella, N. M. (2014). Gravity waves simulated by high-resolution whole atmosphere community climate model. *Geophysical Research Letters*, *41*, 9106–9112. https://doi.org/10.1002/2014GL062468

Livneh, D. J., Seker, I., Djuth, F. T., & Mathews, J. D. (2007). Continuous quasiperiodic thermospheric waves over Arecibo. *Journal of Geophysical Research*, *112*, A07313. https://doi.org/10.1029/2006JA012225

Lund, T. S., Fritts, D. C., Wan, K., Laughman, B., & Liu, H. (2020). Numerical simulation of mountain waves over the Southern Andes. Part 1: Mountain wave and secondary wave character, evolutions, and breaking. *Journal of the Atmospheric Sciences*, *77*, 4337–4356. https://doi.org/10.1175/JAS-D-19-0356.1

Luo, Z., & Fritts, D. C. (1993). Gravity wave excitation by geostrophic adjustment of the jet stream. Part II: Three-dimensional forcing. *Journal of the Atmospheric Sciences*, *50*, 104–115. https://doi.org/10.1175/1520-0469(1993)050<0104:gwebga>2.0.co;2

Makela, J. J., Lognonné, P., Hébert, H., Gehrels, T., Rolland, L., Allgeyer, S., et al. (2011). Imaging and modeling the ionospheric airglow response over Hawaii to the tsunami generated by the Tohoku earthquake of 11 March 2011. *Geophysical Research Letters*, *38*, L13305. https://doi.org/10.1029/2011GL047860

Negrea, C., & Zabotin, N. A. (2016). Mean spectral characteristics of acoustic gravity waves in the thermosphere-ionosphere determined from Dynasonde data. *Radio Science*, *51*, 213–222. https://doi.org/10.1002/2015RS005823

Occhipinti, G., Rolland, L., Lognonné, P., & Watada, S. (2013). From Sumatra 2004 to Tohoku-Oki 2011: The systematic GPS detection of the ionospheric signature induced by tsunamigenic earthquakes. *Journal of Geophysical Research: Space Physics*, *118*, 3626–3636. https://doi.org/10.1002/jgra.50322

Oliver, W. L., Otsuka, Y., Sato, M., Takami, T., & Fukao, S. (1997). A climatology of F region gravity wave propagation over the middle and upper atmosphere radar. *Journal of Geophysical Research*, *102*, 14499–14512. https://doi.org/10.1029/97JA00491

Plougonven, R., & Snyder, C. (2007). Inertia-gravity waves spontaneously generated by jets and fronts, Part I: Different baroclinic life cycles. *Journal of the Atmospheric Sciences*, *64*, 2502–2520. https://doi.org/10.1175/JAS3953.1

Plougonven, R., & Zhang, F. (2014). Internal gravity waves from atmospheric jets and fronts. *Reviews of Geophysics*, *52*(1), 33–76. https://doi.org/10.1002/2012RG000419

Richter, J. H., Sassi, F., & Garcia, R. R. (2010). Towards a physically based gravity waves source parameterization in a general circulation model. *Journal of the Atmospheric Sciences*, *67*, 136–156. https://doi.org/10.1175/2009jas3112.1

Sato, K., Yasui, R., & Miyoshi, Y. (2018). The momentum budget in the stratosphere, mesosphere, and lower thermosphere (2018). Part I: Contributions of different wave types and in situ generation of Rossby waves. *Journal of the Atmospheric Sciences*, *75*, 3613–3633. https://doi.org/10.1175/JAS-D-17-0336.1

Satterfield, E. A., Waller, J. A., Kuhl, D. D., Hodyss, D., Hoppel, K. W., Eckermann, S. D., et al. (2022). Statistical parameter estimation for observation error modelling: Application to meteor radars. In S. K.Park, & L.Xu (Eds.), *Data assimilation for atmospheric, oceanic and hydrologic applications* (Vol. IV, pp. 185–213). Springer. https://doi.org/10.1007/978-3-030-77722-7_8

Smith, S., Baumgardner, J., & Mendillo, M. (2009). Evidence of mesospheric gravity-waves generated by orographic forcing in the troposphere. *Geophysical Research Letters*, *36*, L08807. https://doi.org/10.1029/2008GL036936

Smith, S. M., Vadas, S. L., Baggaley, W. J., Hernandez, G., & Baumgardner, J. (2013). Gravity wave coupling between the mesosphere and thermosphere over New Zealand. *Journal of Geophysical Research*, *118*(5), 2694–2707. https://doi.org/10.1002/jgra.50263

Sutherland, B. R., Achatz, U., Caulfield, C. P., & Klymak, J. M. (2019). Recent progress in modeling imbalance in the atmosphere and ocean. *Physical Review Fluids*, *4*, 010501. https://doi.org/10.1103/PhysRevFluids.4.010501

Taylor, M. J., Pautet, P.-D., Criddle, N. R., Fritts, D. C., Eckermann, S. D., Smith, S. M., et al. (2019). Large-amplitude mountain waves in the mesosphere observed on 21 June 2014 during DEEPWAVE: 1. Wave amplitudes, scales, momentum fluxes, and environmental sensitivity. *Journal of Geophysical Research: Atmospheres*, *124*, 10364–10384. https://doi.org/10.1029/2019JD030932

Vadas, S. L., & Becker, E. (2019). Numerical modeling of the generation of tertiary gravity waves in the mesosphere and thermosphere during strong mountain wave events over the Southern Andes. *Journal of Geophysical Research: Space Physics*, *124*, 7687–7718. https://doi.org/10.1029/2019JA026694

Vadas, S. L., & Fritts, D. C. (2001). Gravity wave radiation and mean responses to local body forces in the atmosphere. *Journal of the Atmospheric Sciences*, *58*, 2249–2279. https://doi.org/10.1175/1520-0469(2001)058<2249:gwramr>2.0.co;2

Vadas, S. L., & Fritts, D. C. (2002). The importance of spatial variability in the generation of secondary gravity waves from local body forces. *Geophysical Research Letters*, *29*(20), 1984–1991. https://doi.org/10.1029/2002GL015574

Vadas, S. L., Fritts, D. C., & Alexander, M. J. (2003). Mechanism for the generation of secondary waves in wave breaking regions. *Journal of the Atmospheric Sciences*, *60*, 194–214. https://doi.org/10.1175/1520-0469(2003)060<0194:mftgos>2.0.co;2

Walterscheid, R., Schubert, G., & Brinkman, D. (2001). Small-scale gravity waves in the upper mesosphere and lower thermosphere generated by deep tropical convection. *Journal of Geophysical Research*, *106*(D23), 31825–31832. https://doi.org/10.1029/2000jd000131

Watanabe, S., Sato, K., Kawatani, Y., & Takahashi, M. (2015). Vertical resolution dependence of gravity wave momentum flux simulated by an atmospheric general circulation model. *Geoscientific Model Development*, *8*, 1637–1644 2015. https://doi.org/10.5194/gmd-8-1637-2015

Witt, G. (1962). Height, structure and displacement of noctilucent clouds. *Tellus*, *14*(1), 1–18. https://doi.org/10.3402/tellusa.v14i1.9524

Yasui, R., Sato, K., & Miyoshi, Y. (2018). The momentum budget in the stratosphere, mesosphere, and lower thermosphere. Part II: (2018). The in situ generation of gravity waves. *Journal of the Atmospheric Sciences*, *75*, 3635–3651. https://doi.org/10.1175/JAS-D-17-0337.1

Yiğit, E., Aylward, A. D., & Medvedev, A. S. (2008). Parameterization of the effects of vertically propagating gravity waves for thermosphere general circulation models: Sensitivity study. *Journal of Geophysical Research-Atmospheres*, *113*, D19106. https://doi.org/10.1029/2008JD010135